2nd of 5 files

Chapters 3 and 4

EFFECT OF STRESS ON INITIATION AND PROPAGATION OF LOCALIZED CORROSION IN ALUMINIUM ALLOYS

By

SUKANTA GHOSH

A thesis submitted to
University of Birmingham
for the degree of
DOCTOR OF PHILOSOPHY
Metallurgy and Materials
School of Engineering
University of Birmingham

November 2007

3 EXPERIMENTAL PROCEDURE

The materials used for this study were predominantly wrought aluminium alloy 2024-T351 along with a cast aluminium-copper binary alloy (i.e., Al-0.099Cu). Compositions of the AA2024-T351 and the cast Al-Cu binary alloy are given in Table 3.1.[5]

Table 3.1 Nominal chemical composition (wt%) of the aluminium alloys used in the present study.

Alloys	Cu	Mg	Mn	Fe	Si	Ni	Cr	Zn	Ti	Al
AA2024-T351	**3.8 - 4.9**	**1.2 - 1.8**	**0.3 - 0.9**	**0.50 max**	**0.50 max**	**-**	**0.06 - 0.1**	**0.25 max**	**0.04 - 0.15**	**Bal**
Al-0.099Cu	**0.099 ± 0.003**	**< 0.0005**	**< 0.0005**	**0.0011 ± 0.0005**	**0.0019 ± 0.0004**	**< 0.0005**	**< 0.0003**	**< 0.0005**	**< 0.0015**	**Bal**

3.1 Sample Preparation (Grinding, Polishing, and Mounting)

All samples used in this current study were polished to a one micron surface finish (unless stated otherwise) irrespective of sample orientation, shape, sizes or type of tests performed. Grinding of the samples was performed through a series of SiC paper (400, 800, and 1200 grit respectively; SiC paper supplied by ‘MetPrep’, UK) in the presence of

---

[5] Composition of the cast binary Al-0.099Cu alloy is obtained from the alloy manufacturer Alcan. Nominal composition of AA2024-T351 is obtained from The Aluminium Association – International Alloy Designation and Chemical Composition Limits for Wrought Aluminium and Wrought Aluminium Alloys, 1998. However, AA2024-T351 used in this current study is similar to that used by Jariyaboon [70] and Doyle [302]. More precise compositional details of AA2024-T351 can be found in their work.

ethanol on the grinding machine. Contact of water during grinding was avoided as water can attack the active ‘S’ phases present in the AA2024-T351 microstructure. Polishing of the 1200 grit-ground samples was performed in 6 μm, 3 μm and 1 μm diamond suspension (i.e., Struers “DiaDuo”) on “Mol” and “Nap” polishing cloths (Struers) respectively. Samples were degreased and cleaned ultrasonically in ethanol for 2-3 minutes between different steps of grinding and polishing. After the final polish to one micron diamond paste and ultrasonically cleaning, the samples were dried using a conventional air blower.

A few samples were also mounted in epoxy resin for large scale ‘in beaker’ electrochemical tests (see Chapter 4) in order to expose only one surface with controlled dimension. An electrical connection was created at the back of the samples with soldered copper wire prior to the mounting of the samples in the epoxy resin. Resin was added in sufficient quantity so that the connection at the back of the sample was completely covered. Met Prep Variset 20 resin was used on these occasions and cured at room temperature for at least 2 hours before electrochemical testing.

3.2 Characterization Techniques (Microstructural and Others)

Several characterizations techniques were used in this current study in order to have a better understanding of the corrosion process associated with different microstructural features. In many cases analysis of different intermetallic particles (as well as intermetallic particle free areas) in AA2024-T351 were performed before and after the electrochemical tests to emphasize the local changes happening during the exposure.

3.2.1 Metallographic Etching

Metallographic etching of the cast Al-0.099Cu binary alloy was performed using an etchant made of 2% HF + 10 % HNO_3 to reveal the cast microstructure of the alloy. The etchant was gently rubbed on the one micron polished sample surface using a cotton bud for approximately 30 seconds and then rinsed with de-ionised water. Whenever required the procedure was repeated for shorter times in order to achieve a clearly visible grain structure. Etching of AA2024-T351 was not performed in this current study but was performed on the same material in other work [70, 302].

3.2.2 Optical Microscopy

Optical microscopy was performed with a Zeiss Axiolab direct microscope with magnifications up to 400X. The optical microscope was equipped with a KS300 3.0 Imaging system (Imaging Associates, UK) for further image analysis. Corroded surfaces were cleaned (i.e., ultrasonically in ethanol, de-ionised water and then dried) prior to the optical micrography.

3.2.3 Scanning Electron Microscopy (SEM)

Electron microscopy was performed using JEOL 6060, 6300, 7000 FEG-SEM (JEOL Instruments, Japan) and a Philips XL-30 (Philips Instruments, UK). The microscopes were used in both secondary and backscattered mode with an accelerating voltage of 15-20 kV and a working distance of 10mm. In most cases, the samples were mounted on aluminium stubs with adhesive carbon tape and silver paint in order to obtain good electrical contact between the samples and the sample holder. All electron microscopes were equipped with an EDX detector for chemical compositional analysis. Analysis of the EDX data was carried out using INCA software (Oxford Instruments, UK). SEMs quipped with EDX were used to perform composition analysis of different intermetallic particles (before and after the electrochemical tests) as well as to document the surface morphology after electrochemical experiments. A Hitachi FEG-SEM (Model S-4000) in conjunction with a 10 kN servo-electric loading stage was used for in situ study of intermetallic particle/alloy matrix delamination as a function of applied stress (see Chapter 6).

3.2.4 Atomic Force Microscopy

Atomic force microscopy (Q-Scope 350 AFM, supplied by Quesant Instrument Corporation, US) in contact mode was used in this current study to characterize the corrosion behaviour of individual intermetallic particles subjected to electrochemical investigation using a micro-capillary electrochemical cell. Morphology of the intermetallic particles and the surrounding matrix were investigated before and after the corrosion (potentiodynamic, potentiostatic or free corrosion/open circuit potential) tests. A maximum scan area of 80 µm × 80 µm and maximum depth of 5 µm was achieved using this set up. A scan rate of 1 Hz was used for good quality images. Analysis of the AFM data was performed using Q-Analysis^{TM} software. It was found that flatness of the samples was very crucial to obtain good tomographic images of the intermetallic particles. Throughout the AFM experiments, care was taken to ensure that the top surface of the specimens remained flat using a leveller. AFM was predominantly used to study the nature of grooving (depth and width of the grooves, discontinuous vs. continuous etc.) around the intermetallic particles during the current study (see Chapter 5 and 6).

3.2.5 Line Profilometry

A Stylet Profilometer DekTak® 6M (from Vecco, US) was used to measure the surface dissolution of AA2024-T351 samples during the surface treatment for ‘S’ phase removal (see Chapter 4). Prior to surface treatment, one part of the sample’s surface (one micron surface finish) was covered with ‘Stop-Off’ lacquer and rest left uncovered. The whole sample was then subjected to surface treatment. After the surface treatment, the ‘Stop-Off’ lacquer was removed and line profilometric analysis was performed at the junction between the surface-treated and untreated areas on the sample. Step heights between these two areas gave an estimation of material dissolution during the surface treatment. A stylet of 2.5 µm radius with a force of 3 mg was used during the profilometric analysis. The length measured was 2000 µm for a total duration of 60 s.

3.2.6 Optical Profilometry

High resolution optical profilometry was carried out with an Altisurf 500 white light profilometer (from Cotec, France) with a sensor having a dynamic range of 50 nm – 300 µm. This technology involves a white light source (quartz-halogen) that is focused onto a sample through a lens that displays a high level of chromatic aberration. The chromatic aberration is then used to precisely measure the position of a particular surface element with respect to a reference point. This non-contact technique can give accurate height information (to a resolution of 5 nanometres) about the 3D surface structure of any material over an area of up to 10 square centimetres. Results were evaluated using Altimap software (see Chapter 5).

3.2.7 Surface Mapping using Microhardness Markers

A microhardness tester was used as a surface mapping tool in this current study rather than measuring the hardness of the material (see Chapter 5 and 6). A Mitutoyo MVK-H1 hardness testing machine (Mitutoyo Ltd, UK) with a load of 100g was used to create the indentation marks. The sample surface (polished to one micron) was marked with a grid of indentations as shown in Figure 3.1. Indentations with a diagonal length of ~ 34 µm (at 100g load) were made at a distance of one mm from each other. An indentation was also created adjacent to the grid for reference. The samples with indentation marks on their surface were subjected to SEM analysis prior to the electrochemical tests. Different types of intermetallic particles (as well as areas without any intermetallic particles) were identified/analysed using EDX and their co-ordinates were noted with respect to their nearest indentation mark.

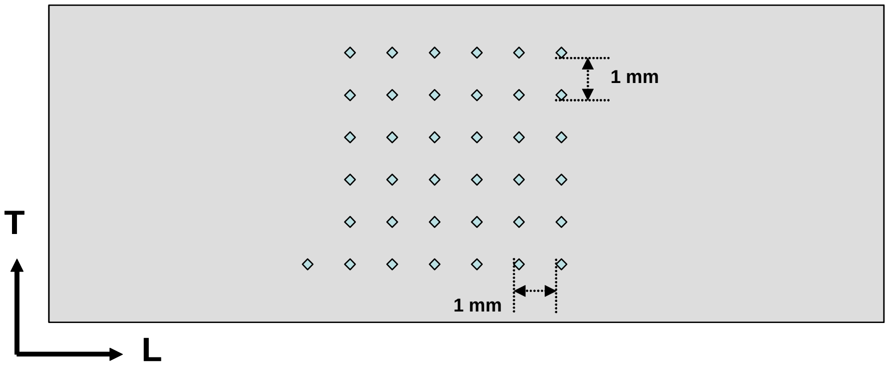

Figure 3.1 Schematic of AA2024-T351 surface mapped with microhardness indentations. Indentations are made at a distance of one mm from each other. One extra indentation is made adjacent to the grid as the reference point. These indentations have a diagonal length of about 34 µm when 100 g load is maintained. L = Longitudinal direction, T = Transverse direction.

After the SEM analysis, the surface mapped samples were lightly polished with one micron diamond paste to remove any possible carbon deposition and contamination on the surface. Relatively deep indentations with 100g load ensured the presence of marks even after light repolishing. This process provided the easier way of particle identification before and after micro-capillary electrochemical cell test. It should be noted that though Fe-Mn particles were visible via optical microscopy, smaller S phase particles were difficult to image using the lower magnification optics attached with the micro-capillary electrochemical cell test set up. After the micro-capillary electrochemical tests (with an exposed area of 40 µm diameter), the exposed intermetallic particles (or the particle free matrix) were again subjected to SEM and EDX analysis based on their previously determined co-ordinate position with respect to the nearest microhardness markers.

3.3 Surface Treatment

Prior to the surface treatment, all samples were finally polished to one micron surface finish as described in Section 3.1. Polished samples were then degreased with methanol in an ultrasonic bath for 2 minutes. For the standard surface treatment, the samples were etched in 3g/l sodium hydroxide (NaOH) for 10 minutes, rinsed under running tap water for 2 minutes, desmutted for 30s in nitric acid [i.e., 1:2 (vol) of water : 70% nitric acid] and finally rinsed for 5 minutes under running tap water. In some cases (whenever necessary), 10 mM $CeCl_3$ salt was added in the nitric acid while desmutting.

3.4 Electrochemical Tests with 'Large' Exposure Area ('In Beaker Cell')

3.4.1 The Samples

Samples of 35 mm length and 3 mm width were cut from a six mm thick AA2024-T351 plate as shown in Figure 3.2. All experiments were performed on the SL plane of the samples as indicated in the figure. One micron surface finish was used for all experiments unless stated otherwise. Exposed areas of the samples were controlled by lacquering (with 'Stopping Off' lacquer) the surface. Exposed areas were varied from 1.2 cm^2 (24 mm × 5mm) to as small as 0.01 cm^2 (1 mm × 1 mm) depending on the experiments performed (see Chapter 4). A few samples were mounted in epoxy resin by the process described in Section 3.1. Areas between the sample edge and the epoxy resin were lacquered to avoid any crevice corrosion. In all cases lacquer was applied in several layers and dried completely prior to any electrochemical tests.

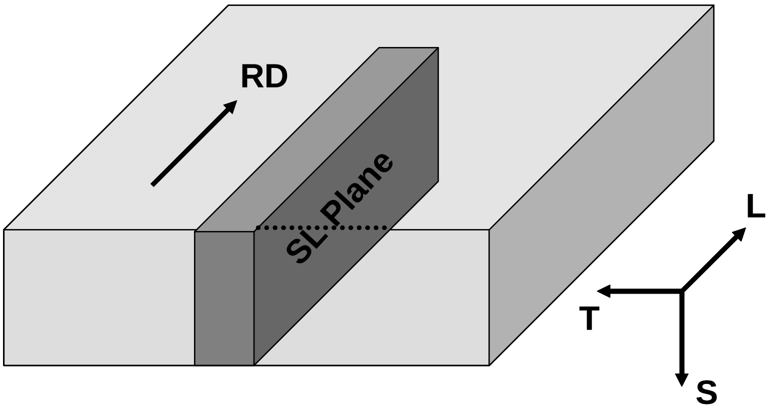

Figure 3.2 Schematic of a specimen used in 'large' exposure area electrochemical experiments. Specimens are cut from a six mm thick AA2024-T351 plate. All experiments are done in SL plane. RD = Rolling Direction, L = Longitudinal Direction, T = Transverse Direction, S = Short Transverse Direction.

3.4.2 Electrochemical Cell

A special glass vessel (Figure 3.3) with five opening in its lid was used to perform electrochemical tests (i.e., anodic and cathodic polarization scans, short term open circuit tests) in both naturally aerated and deaerated conditions (see Chapter 4). The five openings in the glass lid were used to position sample, counter electrode, reference electrode, gas inlet and gas outlet. For all tests, a standard calomel electrode (SCE) and a platinum mesh were used as reference and counter electrode, respectively.

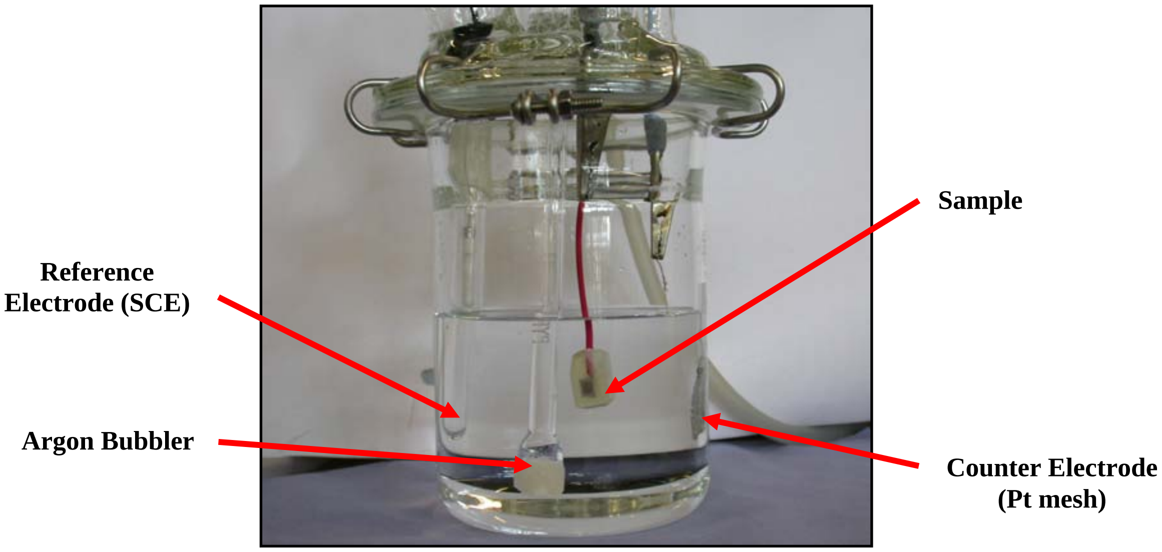

Figure 3.3 Glass cell for performing electrochemical experiments with large exposure area.

3.4.3 Deaeration of the Electrochemical Cell

Argon (BOC gases, UK) gas was purged through the bubbler (see Figure 3.3) for deaerating the solution (10 mM NaCl in this case). However, in order to have consistency between different potentiodynamic and potentiostatic tests in deaerated condition (see Chapter 4), it was essential to know the approximate purging time for achieving maximum deaeration utilising the current electrochemical set up. Quantification of the degree of deaeration was achieved through a series of potentiodynamic and potentiostatic tests in 10 mM NaCl using Pt as a working electrode. Firstly, cathodic polarization scans were performed on a Pt working electrode in a naturally aerated condition (Figure 3.4a). The oxygen reduction plateau was observed between -100 mV and -825 mV vs. SCE with a diffusion limited current density of ~ 100 $\mu A/cm^2$. A potential in the middle of the oxygen reduction plateau (- 500 mV vs. SCE in this case) was then chosen for further potentiostatic tests (Figure 3.4b). Purging of the Ar gas through the solution was continued during the potentiostatic polarization and change in the current density was observed as a function of deaeration time. Cathodic current density decreased with the increase in the deaeration time. It can be seen from Figure 3.4b that the cathodic current reached a stability region after 20 minutes of deaeration. After about 2900 seconds, argon purging was stopped but the potentiostatic test was continued. It can be seen from the Figure 3.4b that the current density stayed approximately the same for the reminder of the test without argon purging.

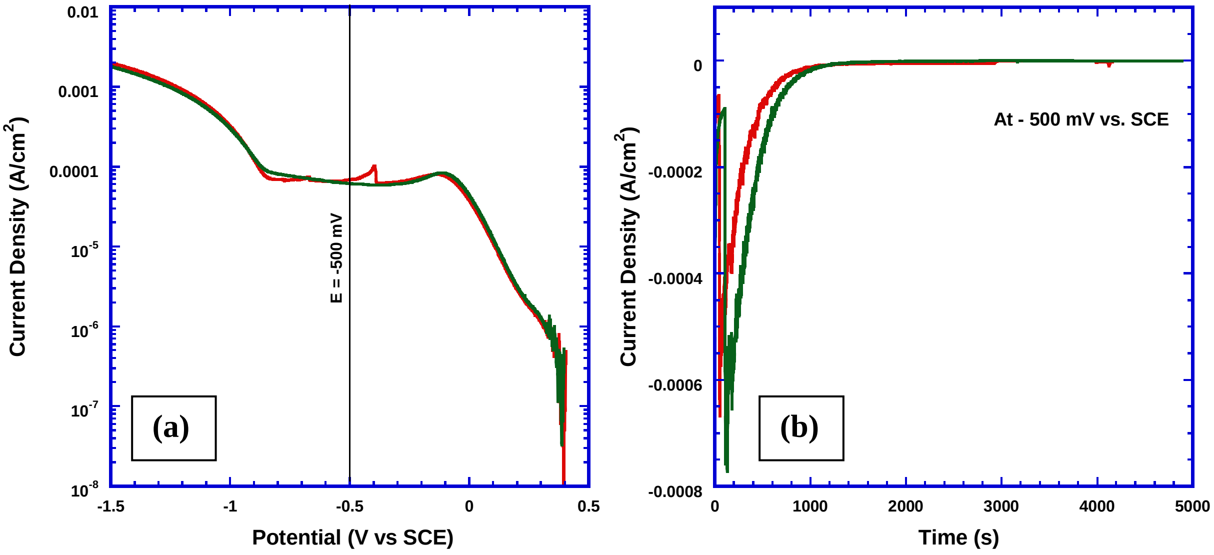

Figure 3.4 Electrochemical tests for checking complete deaeration of the experimental cell. (a) Cathodic potentiodynamic scans of Pt working electrode in naturally aerated 10 mM NaCl. (b) Potentiostatic polarization of Pt working electrode during deaeration (with Argon) in 10 mM NaCl. A potential (- 500 mV vs. SCE) from the middle of the oxygen reduction plateau was chosen for potentiostatic polarization.

These above mentioned tests ensured maximum deaeration of the solution using the current experimental set up. However, during the actual tests with AA2024-T351 specimens, argon was purged through the 10 mM solution for about 50 minutes in order to minimise the presence of any residual oxygen. AA2024-T351 specimens were kept above the solution inside the closed cell during deaeration and were pushed into the solution before beginning of the electrochemical tests at the end of argon purging. At the end of 50 minutes of purging, the argon bubbler was lifted just above the solution level and kept purging with a very slow flow rate. This ensured the presence of argon blanket inside the cell during the electrochemical tests.

3.4.4 Potentiodynamic Polarization Experiments

Potentiodynamic polarization experiments were carried out utilising a Solartron 1280 or 1285 potentiostat controlled via computer through CorrWare V2.0 software.

3.4.4.1 Anodic Polarization Scans

Anodic polarization scans were performed on one micron surface finished AA2024-T351 samples in both surface treated and untreated conditions at room temperature. 10 mM NaCl solution in naturally aerated and deaerated conditions was used to perform the test. Scans were started at 20 mV negative to the open circuit potential and continued with a scan rate of 1 mV/s to the anodic (i.e., positive) direction. Prior to the start of the experiment, samples were held at open circuit for one to five minutes depending on the stability of the potentials.

3.4.4.2 Cathodic Polarization Scans

The cathodic polarization scans were performed in naturally aerated 10 mM NaCl as well as in different buffer solutions at room temperature (see Chapter 4). Scans were started at 20 mV positive to the open circuit and continued with a scan rate of 1 mV/s to the cathodic (i.e., negative) direction until -1.8 V vs. the reference. Buffer solutions [171, 303] used in the experiments were:

i) 0.1 M H_3BO_3 adjusted to pH 7 by the addition of 1 M NaOH
ii) 0.1 M Na_2HPO_4 adjusted to pH 7 by 4 M H_3PO_4

3.4.5 Potentiostatic Polarization Experiments

Samples were polished to one micron and surface treated as required. In a few cases 800 grit surface finish were also used as rough surface were thought to enhance the possibility of detecting metastable activities by increasing its frequency of occurrence. However, at any given potential, comparison of the corrosion properties between the surface treated and untreated samples were always made under similar surface finishing. Different sample areas (i.e., from 1.2 cm^2 to as small as 0.01 cm^2) were used to capture the metastable pitting transients. These experiments were also carried out with Solartron 1280 or 1285 potentiostat operating with CorrWare V2.0 software.

All the tests were performed in 10 mM NaCl solution either in naturally aerated or deaerated condition at room temperature (see Chapter 4). Based on the anodic polarization scans different potentials were chosen for further potentiostatic polarizations. Potentials were varied from -575 mV vs. SCE (in the passive region) to -500 mV vs. SCE (close to pitting potential) to find transients correspond to metastable pitting. The data was collected at a frequency of 10 Hz (10 points/s). Higher the frequency of data collection ensured a greater chance to capture each transients and obtaining a smooth curve. Samples were inspected in optical as well as under SEM to identify and quantify in size the metastable and stable pitting associated with the electrochemical data.

3.4.5.1 Calculation of Metastable Pit Size from Charge Passed

The size of a single metastable pit was calculated from a single current transient using Faraday's law and assuming hemispherical pit geometry. The charge passed during the time from metastable pit initiation to the peak pit current or from pit initiation to its repassivation was calculated using the KaleidaGraph® (version 4.0) software (Figure 3.5) [134]. From the charge of each event, apparent metastable pit sizes at peak pit current and total size of the metastable pit were calculated using the Faradaic relationship assuming hemispherical pit geometry (Equation 3.1):

$$r_{pit} = \left[\frac{3AW}{2\pi zF\rho}\right]^{1/3}\left(\int_{t_i}^{t_{\max}}\left(I_{app} - I_{OX}\right)dt\right)^{1/3}$$ **Equation 3.1**

where r_{pit} is the pit radius, AW is the atomic weight, z is the valence, F is the Faraday's constant, ρ is the density, I_{app} is the anodic current, I_{OX} is the passive current, t_i is initiation time, t_{max} is the time at which i_{peak} is reached and t_f is the time of repassivation of the metastable pit. To calculate the total pit size (including the time of repassivation), the charge could be calculated from t_i to t_f.

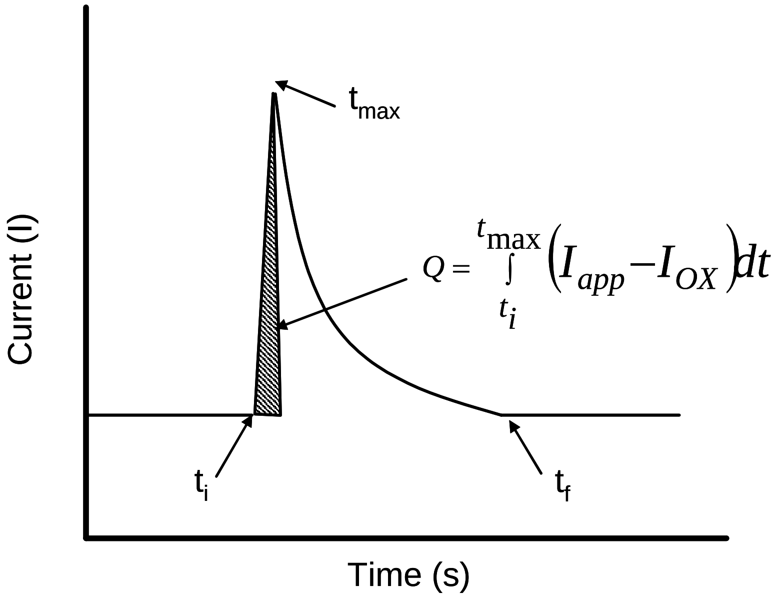

Figure 3.5 Schematic showing the limits of numerical integration of a metastable pitting event.

3.4.5.2 Potentiostatic Experiments to Investigate the Role of Oxygen in Metastable Pitting

Schematic of the experimental set up for investigating the role of oxygen in metastable pitting is shown in Figure 3.6. Potentiostatic polarization scans were performed at -520 mV vs. SCE on one micron polished AA2024-T351 samples etched in NaOH and desmutted in HNO_3+10 mM $CeCl_3$. The exposed sample area was ~ 0.0375 cm^2 and all tests were performed in 10 mM NaCl at room temperature (see Chapter 4).

The electrochemical cell (marked as ‘A’ in Figure 3.6) was filled with ~ 500 mL and the conical flask (marked as ‘B’) was filled with ~ 300 mL of 10 mM NaCl solution, respectively, before the beginning of each test. Both these cells were deaerated following the same procedure as described in Section 3.4.3. After purging Ar through the electrochemical set up for 50 min, both the stopper (position ‘1’) and the gas cylinder valve were closed. The gas inlet (position ‘2’) was detached from the stopper (position

‘1’) and attached with the gas outlet (position ‘3’, after removing it from the water beaker labelled as ‘C’) of the conical flask.

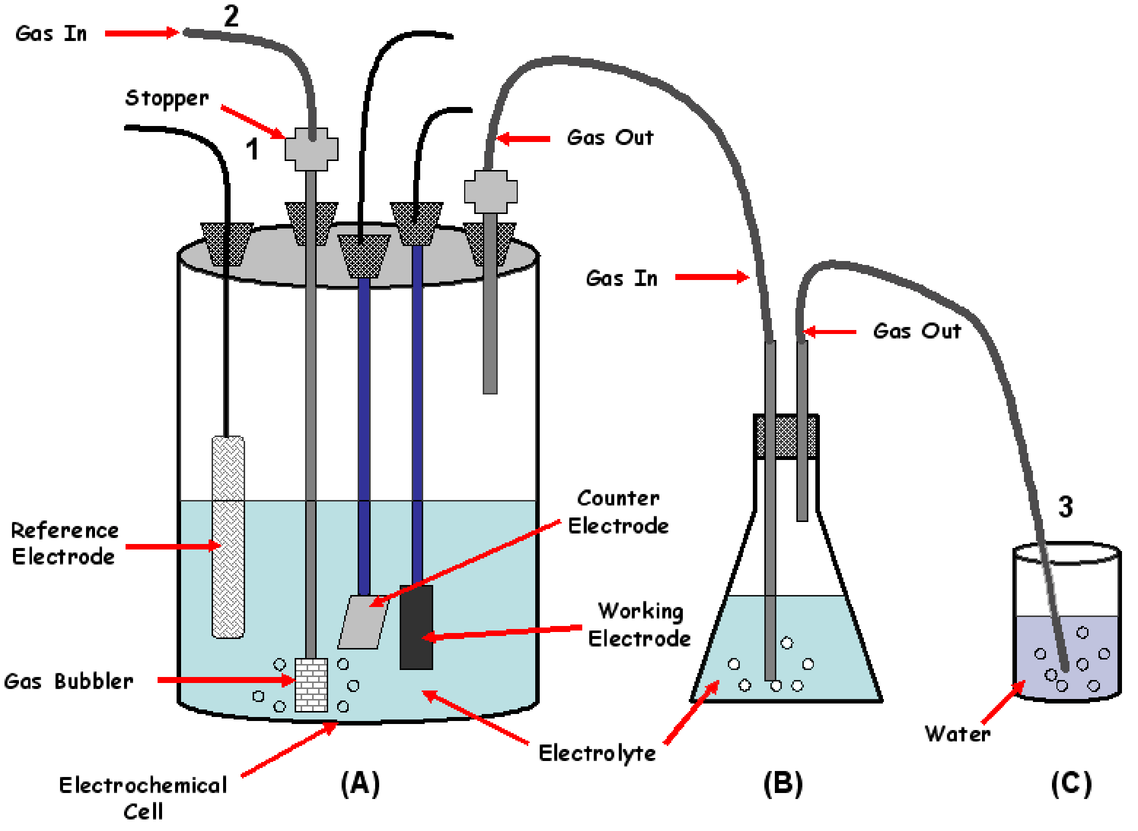

Figure 3.6 Schematic of the experimental set up used for the electrochemical experiments to investigate the role of oxygen in metastable pitting. (A), (B), and (C) respectively represent the electrochemical cell, conical flask, and beaker that are used during the test. Position 1, 2, and 3 can be interchanged during the course of test to introduce deaerated or aerated solution in the system as required.

The potentiostatic experiment was started and as soon as the metastable pitting was observed (or started appearing as the transients in the curve), the gas cylinder was opened and gas flow was allowed at a slow rate. This argon flow transferred the deaerated solution from the conical flask ‘B’ to the electrochemical cell ‘A’. After about 100s of potentiostatic hold, ~ 100 mL of deaerated solution was transferred to the electrochemical cell ‘A’. Aerated solution (prepared in a separate glass vessel by passing air through the solution for 40 minutes) was added in the electrochemical cell with a syringe through the port used for the gas bubbler. Two batches of aerated solution were added at different time intervals during the experiment with a quantity of 100 mL and 150 mL, respectively. Both deaerated and aerated solution during the experiment was introduced in the system with minimum of agitation.

3.4.6 Open Circuit Potential (OCP) Measurements

Open circuit potential (also referred as corrosion potential) tests of one micron polished AA2024-T351 samples were performed in naturally aerated 10 mM NaCl in both as-received and surface treated conditions at room temperature. Open circuit potentials of these samples were measured either for a short time period (i.e., 15-30 minutes) or over a longer period (i.e., 3-4 days).

Solartron potentiostats (1280 or 1285) were used to collect the open circuit potentials of the samples during the short duration exposure (i.e., 30 mins) in the beaker cell (as shown in Figure 3.3). Epoxy resin mounted samples were used for long term open circuit tests which were performed for 3-4 days by immersing the samples in conventional beakers containing ~ 500 ml of naturally aerated 10 mM NaCl solution. These beakers were immersed in a thermal bath maintained at 25˚C in order to control the thermal fluctuations during the day-night continuous exposure. Corrosion potentials (OCP) of these samples were monitored using a Keithley data logger Multimeter (Model 2000, Keithley Instruments, UK) with up to 10 channels being recorded simultaneously.

Analysis of the data was carried out using ‘Testpoint’ software. All the experiments were repeated at least twice. After the long exposure, the samples were severely corroded and developed a white corrosion product on the surface. Although concentrated HNO_3 (70%, 15.8 N) was used to clean the surface [304], white scale was not removed totally even after three hours of immersion,. Metallographic analyses of the samples were done using optical microscope.

3.5 Micro- Capillary Electrochemical Cell Testing

The capillary based microelectrochemical cell technique is now well established and widely used in the field of electrochemical studies of the surfaces [16, 17, 30, 32, 33, 40-42, 305-310]. Very small exposure of the surface (as low as 1-5 µm diameter) during the micro-capillary electrochemical tests allow selective measurements of the area of interests (e.g., inclusions, precipitations, intermetallic particles, grain boundaries, or single heterogeneities in structure.).

The original idea of this new micro-capillary electrochemical cell technique (often referred as ‘microcell’ technique) was developed by Suter and Böhni [16]. The experimental setup for the microelectrochemical cell is based on the standard three electrode arrangement consisting of a counter, reference, and working electrode (Figure 3.7). The microcapillary cell used in this present study was slightly modified from the original microcell design used by Suter and Böhni [16]. Conventionally, the reference electrode is placed at some distance away from the microcell connected through an electrolytic path. In this current study, the reference electrode (Ag/AgCl in this case) was directly inserted in the microcell, as can be seen in Figure 3.7. This slight modification in the microcell design allowed experiments to be performed at lower concentration (0.1 M NaCl) compared to the conventional microcell setup (0.5 M NaCl was the lowest concentration possible in the conventional microcell setup possibly due to the IR drop related issues).

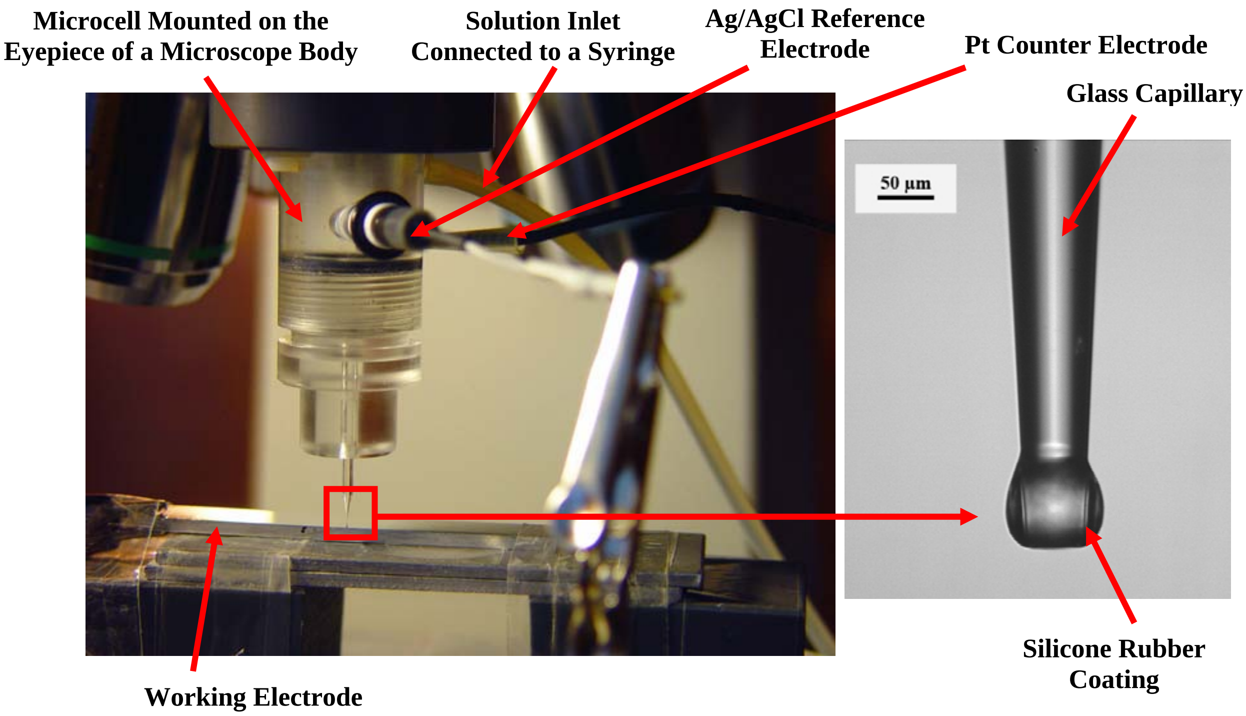

Figure 3.7 Micro-capillary electrochemical cell test setup. The cell setup is based on the standard three electrode arrangement, incorporating a counter, reference and working electrode. The working area is defined by the diameter of the microcapillary tip which is generally coated with silicone rubber to avoid solution leakage.

The microcapillary was filled with solution which provided an electrolytic path to the counter and reference electrodes. A tube connected with a syringe served as solution inlet to the microcell. The syringe attached with the microcell provided easy option for solution flushing through the microcapillary and therefore refreshing the system after each test. Normally the microcapillary is made of glass and its grounded tip is coated with silicone rubber to prevent any leakage of electrolyte. The deformability and the hydrophobic behaviour of the silicone rubber provides major advantages during electrochemical measurement [17]. Excellent deformability of the silicone rubber permits testing on a rough surface and the hydrophobic nature of silicone prevents formation of crevices due to solution leakage under the seal.

Throughout this current micro-capillary electrochemical study (see Chapter 5 and 6), capillary tip diameter of was maintained at 40 µm (i.e., equivalent exposure area of 40 µm diameter). These microcapillaries were prepared by heating and pulling a borosilicate glass capillary (Harvard Apparatus, 2.0 mm outer diameter and 1.16 inner diameter) using a capillary puller (Narishige) once the melting temperature of the borosilicate glass was reached. The pulled capillaries were then ground in 4000 grit SiC paper in the presence of a lubricant (glycerine in this case) till the desired capillary diameter was reached. Polished glass capillaries were then cleaned with ethanol, dried and coated with silicone rubber (RS 555-588 Silicone Rubber Compound, RS Components, Northants, UK). A stream of ethanol was passed through the microcapillary in order to flush out the silicone inside the capillary without destroying the fine tip and silicone rubber skirt. A relatively thick layer of silicone (normally the thickness of the silicone layer at the capillary tip was equivalent to one-fifth of the capillary tip diameter) was applied to the capillary tip by repeating this process several times. As the silicone cured very slowly, an interval of about 30 min was maintained between two consecutive coatings to ensure hardening of each layer. Microcapillaries coated with silicone were stored overnight prior to their use in the microcell.

The fully assembled micro-capillary electrochemical cell setup along with reference and counter electrode was then fixed at the revolving nosepiece on an optical microscope, replacing an objective (Figure 3.7). The specimen was mounted on the microscope stage. This arrangement enabled the search for a microstructural site utilising different magnifications before switching to the microcapillary. It also allowed precise positioning of the capillary on the area of interest. The microscope was attached with a camera which allowed imaging of the surface under investigation before and after the tests. The entire micro-capillary electrochemical cell setup was placed in a Faraday cage to avoid any noise disturbance from adjacent equipment. Detailed discussion about the micro-capillary electrochemical cell technique including capillary preparation can be found elsewhere [17].

The micro-capillary electrochemical setup used in this study was connected to a low noise CH potentiostat (CH Instruments, Model CHI600B) or with a modified high-resolution potentiostat with a current detection limit of 20 fA (Jaissle Electronik GmbH, Waiblingen, Germany 1002T-NC-3).[6] Specimens used in this study were mechanically ground by SiC papers (from 400 to 1200 grit) and polished with several grades of diamond suspensions (from 6 µm to 1 µm). During grinding, sample contact with water was avoided by using ethanol as a lubricant (as water can partially attack the S phases which were later electrochemically tested). Detailed description of grinding and polishing has been given earlier. Samples were cleaned ultrasonically in ethanol for 2-3 minutes between different steps of grinding and polishing. After the final polish to one micron diamond paste and ultrasonically cleaning, the samples were dried using a conventional air blower.

It was found that the time between the final polishing and performing the micro-capillary electrochemical tests were crucial. So, after final polishing, samples were kept 1.5 – 2 hours in air before starting the tests. All tests on a single specimen were

---

[6] Microcapillary electrochemical cell experiments with the ‘Jaissle’ potentiostat were performed in the LRRS, Université de Bourgogne, Dijon, France as a part of an International collaboration funded by the Royal Society, UK.

performed on the same day as it was found that leaving the sample overnight sometime gave problem in running the tests.[7] Naturally aerated NaCl solution of 0.1 M and 0.5 M concentration was used in the micro-capillary electrochemical tests. All experiments in the microcapillary electrochemical cell were carried out at room temperature. All potentiodynamic scans were started at a specified potential (-1000 mV, -800 mV, -700 mV vs. Ag/AgCl etc.) without any delay at open circuit potential. The scan rate (or sweep rate) for all potentiodynamic scans was set at 1 mV/s. The controlling computer programs were set in such a way that, the potentiodynamic experiments were terminated once the current reached a value of 10 nA.

In many cases, microhardness markers were used to identify specific intermetallic particle location. These markers helped in finding the particles on the specimen surface and made capillary positioning easier. The compositions of those intermetallic particles were confirmed using EDS analysis. After SEM and EDS investigations the surface mapped specimens (i.e., array of microhardness markers 1 mm apart from each other on the specimen surface along with identified areas of interest with respect to the grid markers – see Section 3.2.7) were lightly polished in one micron diamond paste prior to the micro-capillary electrochemical tests.

---

[7] Samples stored overnight sometimes showed problem in creating proper contact (which was necessary to run the electrochemical test) between the capillary and the specimen. Sometimes the potentiodynamic scans showed almost a constant cathodic current and sudden breakdown without showing any definite open circuit potential and passive region.

3.6 Mechanical Tests Associated with Stress Assisted Localized Corrosion Studies

3.6.1 Mechanical Testing of AA2024-T351

Tensile samples were made from the mid-plane of a rolled AA2024-T351 plate of 6 mm thickness. The rolled plate was milled on both faces to make the samples approximately 3 mm thick. Samples were cut in such a way that the applied stress was parallel to the rolling direction of the plate. The gauge length of the samples was fixed to 40 mm whereas the width of the specimen was 15 mm. Samples were ground to 1200 grit sand paper to ensure a smooth surface finish. A Zwick 1484 twin screw re-circulating ball universal tensile tester with a 200 kN (dynamic ± 200 kN) load cell mounted on an X-head was used for the tensile tests. As the specimens were flat, 100 kN Instron strip grips mounted axially in the load train were used during the course of experiment. The cross head speed of the tensile machine was maintained at 1 mm/min and this speed yielded a strain rate of 4.17×10^{-4} s^{-1}. Each experiment was carried out until the specimen fractured (see Chapter 6). A PC based data acquisition system was used to control the machine operation and data recording. Raw data was taken out, plotted, and analysed using ‘KaleidaGraph’ software. Elastic modulus (E), proof stress at 0.2% strain (referred as Yield Stress in this current study), stress at maximum load (ultimate tensile strength) and strain at fracture was calculated for each specimen of AA2024-T351. Tensile tests were also performed on a sensitized temper of AA2024 (i.e., heat treated at 250˚C for 2 h, followed by water quenching) in similar manner.[8]

---

[8] In this case, stress was applied perpendicular to the rolling direction.

3.6.2 Four Point Bend Stressing Set Up for In Situ SEM Studies

Samples were prepared from the middle section of a 6 mm thick plate of AA2024-T351. Top and bottom faces of the plate were milled first and then samples with 34.5 mm length, 10 mm width and 3 mm thickness were manufactured from it using a diamond blade cutter (Figure 3.8). Samples were cut in different orientations such that stress could be applied parallel and perpendicular to the stressing direction. Samples were then polished to 1 micron diamond surface finish and finally polished with colloidal silica.

A four point bending set up was used (Figure 3.9) in the stressing stage for in situ[9] study using a high resolution Hitachi FEG-SEM (Model S-4000). The applied load using this four-point bend set up was calculated using Equation 3.2.

$$P_{\max} = \frac{\sigma_{\max} W T^2}{3a}$$ **Equation 3.2**

where, P = Applied load, σ = Stress, W = Width of the specimen, T = Thickness of the specimen, and a = 9 mm in this case.

It was very difficult to control the effective load using the load cell attached with the four-point bend test set up in the servo electric stressing stage. It has also to be noted that the load cell on the servo electric stressing stage is calibrated for tensile-tensile loading and not for four-point bend set up. Hence, a strain gauge was used to calculate the applied stress (as a percentage of yield stress) more precisely. Tokyo Sokki Kenkyuyo FLK-1-23 strain gauges (3 mm long and 1 mm wide) were mounted on the top surface of

---

[9] In these in situ experiments, stress was applied on the sample during the SEM analysis (i.e., when the sample mounted on the stressing stage was actually inside the vacuum chamber of the microscope).

the sample using superglue (Figure 3.8). After firmly fixing the strain gauge to the surface, it was coated with silicone rubber to prevent the superglue from dissolving during the final stage of cleaning with ethanol.

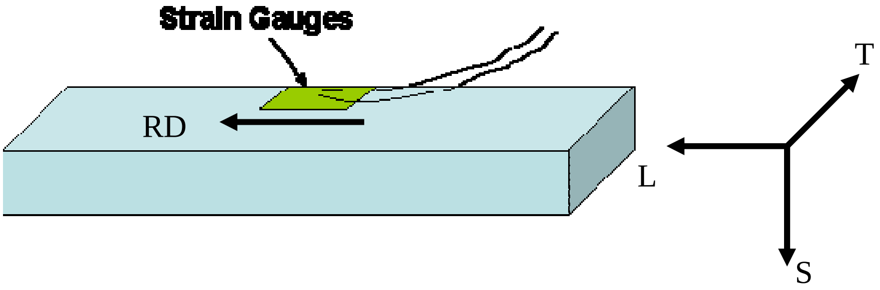

Figure 3.8 Orientations of the specimen prepared from the AA2024-T351 rolled plate. RD = Rolling Direction, L = Longitudinal Direction, T = Transverse Direction, S = Short Transverse Direction. Load is applied parallel or perpendicular to the rolling direction. Observations are made on the L-T plane of the sample. Strain gauge is fixed on the top of the surface.

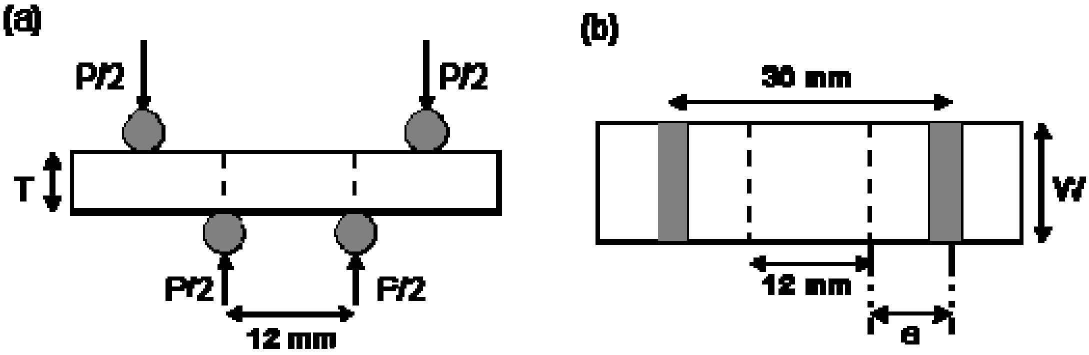

Figure 3.9 (a) Longitudinal Section and (b) Top view of four point bending arrangement used in the present study. P = Load Applied, T = Thickness of the sample, W = Width of the sample, a = 9 mm in this case.

Calibration of a strain gauge was performed via the application of known loads in an Instron machine (Instron 8501 with a servo-hydraulic frame and a 10 kN load cell mounted axially on the upper fixed X-head) using the same type of four-point bend set up. The machine was equipped with a digital control system. During the calibration, the strain gauge was connected to a strain indicator (P-3500, Measurements Group - Instrument Division, US). Load was applied gradually through the instron and the corresponding strain value was noted from the strain measuring unit. A typical load-elongation curve obtained during the calibration is shown in Figure 3.10.

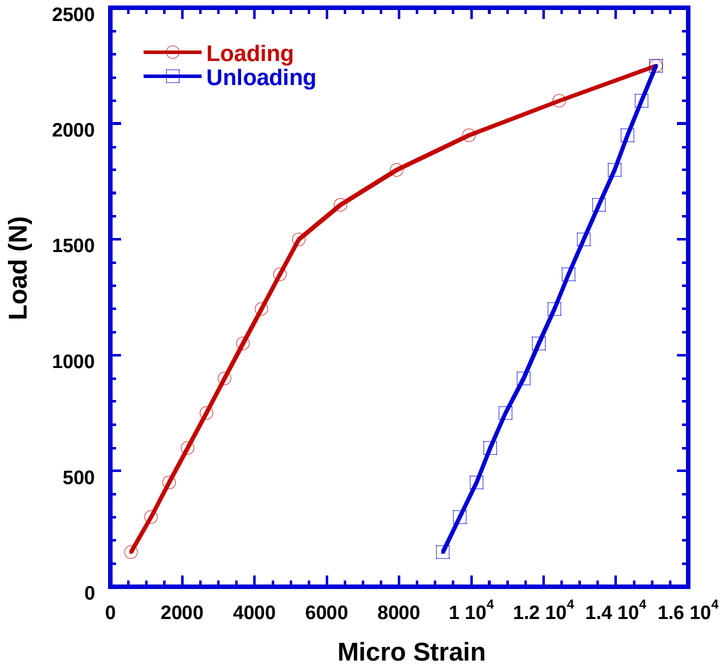

Figure 3.10 A typical load-strain curve for the AA2024-T351 samples during the calibration of the strain gauge using known load. Sample was stressed in the four point bend test set up using Instron machine.

The calibration curve shows high strain value after unloading as the sample was stressed beyond its yield strength. Using the width and thickness of any particular specimen each load on this curve can be represented as the percentage of yield strength of

AA2024-T351. For example, using four-point bending stage geometry, load required to reach the 90% of the yield strength (Y.S. ~375 MPa) for a particular AA2024-T351 sample was calculated to be about 1250N. The calibration curve showed the strain value at this load as 4130e-06. During the in situ FEG-SEM experiments using the servo-electric stressing stage, the sample was strained until the strain gauge output showed the value of 4130e-06. This ensured any desired stress level in the specimens irrespective of the load value read from the load cell.

3.6.3 FEG-SEM Observations Under In Situ Applied Stress

After the strain gauge was mounted on the specimen and silicone rubber was fully cured, the specimen was loaded. It is important to measure the sample dimension prior to its loading in the stage as any inaccurate measurement would result in to the wrong calculation of load. Generally a strain gauge mounted on the sample surface and coated with silicone rubber was left in air for 5-6 hours to ensure complete drying of the silicone rubber. After this procedure, the sample was loaded in a 10 kN servo-electric loading stage (Figure 3.11) for in situ analysis in the FEG-SEM. Following placement of the loading stage within the SEM specimen chamber, the SEM was kept under vacuum overnight to ensure a good vacuum prior to the start of the test. Inside the SEM the load is gradually applied and normally controlled by the mechanical device attached to the stage. However, the actual magnitude of the load was determined from the value shown by the external strain measuring device which was attached to the strain gauge. It has to be noted that no EDX analysis was available on this machine. Details of different load levels and number of intermetallic particles analyzed will be discussed further in Chapter 6.

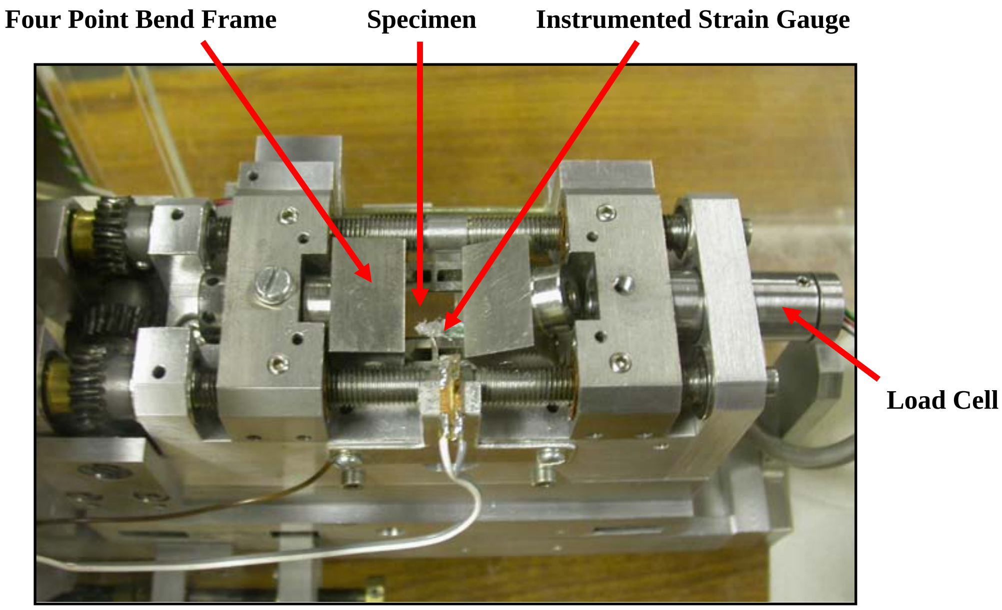

Figure 3.11 Four-point bend test set up with 10 KN servo electric loading stage.

3.7 Electrochemical Testing with an Applied Stress

3.7.1 Capillary Cell Electrochemical Studies Under Applied Plastic Stress Using a 3-point Bend Set Up

Local electrochemical measurements in combination with a 3-point bending frame were used to investigate the effect of applied plastic stress on the corrosion properties of aluminium alloys. Local electrochemical measurements were performed on the L-T plane of the wrought AA2024-T351 samples as well as on the cast Al-0.099Cu binary alloy. AA2024-T351 samples were prepared in similar fashion as described for the four-point bend in situ/SEM tests. The cast binary alloy was provided in the form of a 10 mm thick plate. The top and bottom faces of the 10 mm thick plate was milled first and then samples with 34.5 mm length, 10 mm width and 3 mm thickness were cut from it using diamond blade cutter. All samples were polished to one micron diamond surface finish, rinsed in deionised water, ultrasonically cleaned in ethanol and dried prior to the test following similar procedure described earlier.

Freshly polished sample shows some variability during the potentiodynamic scans possibly due to the relatively unstable passive film on the surface. It was earlier reported that leaving the polished sample in air for one day might bring some consistency in the potentiodynamic scans in the unstressed condition [311]. This delay after polishing ensures that the formation of the oxide film developing on the fresh metal surfaces has reached its stable state. However, the delay after polishing do not influence the conclusions derived from the potentiodynamic tests on unstressed vs. stressed samples. Throughout this whole study, the time between the polishing and performing tests was noted for each test.

Figure 3.12 shows the capillary cell electrochemical test set up. Except the differences in the capillary, the capillary cell method is similar to that of the micro-capillary electrochemical cell (as described in Section 3.5). Instead of a 40 µm diameter glass capillary (as used in micro-capillary electrochemical cell - Section 3.5), an approximately 1 mm diameter pipette (plastic pipette Finntip 60, supplied by Aldrich; with an exposure area of 1.2 mm^2) was used in the capillary cell used. The local cell assembly (Figure 3.12) consisting of a pipette tip, a Pt wire counter electrode and Ag/AgCl reference electrode was linked with a ‘GillAC’ ACM potentiostat or a “Field Machine” potentiostat or a low noise potentiostat (CH Instruments, Model CHI600B).

Electrochemical tests were performed in naturally aerated 0.01 M or 0.1 M NaCl solution at room temperature. Before the polarization, open circuit potential (OCP) of the exposed area was monitored for 60-300 seconds. After the initial hold, anodic polarization was started at a negative potential of 50 mV (i.e., 50 mV in the cathodic domain) with respect to the OCP. Scan rate for all the experiments were 1 mV/s.

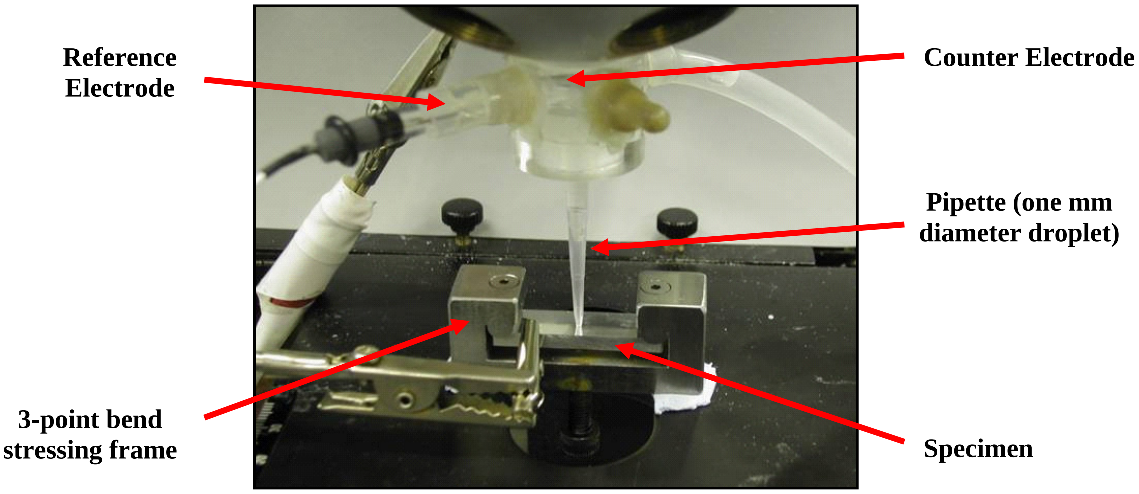

Figure 3.12 The capillary cell electrochemical test setup consists of a three electrode cell within a fine pipette mounted on an optical microscope body.

Samples were first placed in the 3-point bend setup without any application of stress and potentiodynamic scans were performed. Once a set of anodic polarization experiments were finished on the unstressed samples, stress was applied to the samples and further electrochemical testing was performed. Using the 3-point bend set up, samples were plastically stressed parallel to the rolling direction[10] beyond their yield strength and the pipette was place at the point of maximum deflection of the sample (Figure 3.13).

Strain gauges were places on the samples to have an estimation of the strain level. The strain gauge failed after the deflection at the midspan of the AA2024-T351 sample in 3-point bend set up reached 1.3 mm with a strain value of ~ 48000e-06 (i.e., 4.8%). Similar type of stain gauge failure was also observed for Al-0.099Cu cast binary alloy. Placing a strain gauge on the sample surface limits the available space for performing

---

[10] However, in the earlier work [36] identical electrochemical behaviour was observed of the samples stressed in different orientation [i.e., stressed AA2024 samples show similar electrochemical behaviour irrespective of the applied stress orientation (perpendicular or parallel to the rolling direction)].

electrochemical experiments. So, to maintain the equivalent stress level for all the tests, all samples were subjected to midspan deflection of 1.6 mm (i.e., strain > 5%). It should be noted that, the strain level for the capillary cell electrochemical tests using 3-point bend set up was much higher than the in situ FEG-SEM tests for particle delamination using 4-point bend set up. The maximum strain in 4-point bend tests was 0.9% where as in 3-point bend tests strain level was always > 5%.

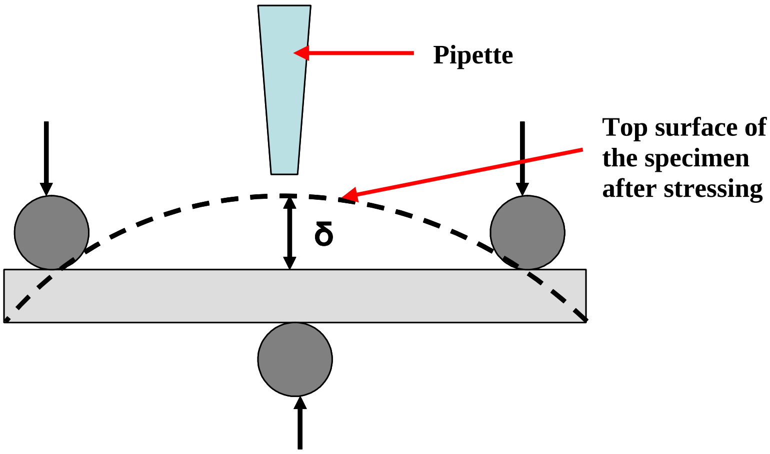

Figure 3.13 Schematic of the capillary cell electrochemical test set up combined with the 3 point bend stressing frame. The midpoint deflection (δ) after stressing was kept constant at 1.6 mm for all experiments. Pipette for local electrochemical tests in stressing condition was always put at the point of maximum deflection.

3.7.2 Capillary Cell Electrochemical Studies Under Applied Elastic Stress Using Tensile Stage

This section describes the electrochemical tests performed on elastically stressed AA2024-T351 samples. Specimens were taken from the middle section of a 6 mm thick plate of AA2024-T351 and given the shape of a tensile specimen by machining as shown in Figure 3.14. Load was applied parallel to the rolling direction of the plate. Sample preparation and the local electrochemistry set up (capillary cell, exposed area ~ 1.2 mm^2) were similar to that of described in Section 3.7.1. All measurements included in this section were performed using a low noise potentiostat (CH Instruments, Model CHI600B). AA2024-T351 specimens were stored in air at least one day after polishing to ensure a stable passive film on the specimen surface.

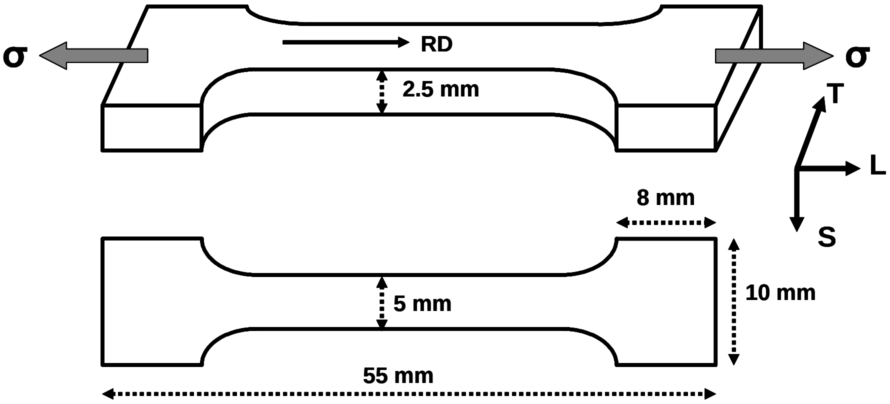

Figure 3.14 Schematic of a typical tensile specimen used in the motorized tensile module in conjunction with the local microelectrochemical tests. Load was applied parallel to the rolling direction. RD = Rolling Direction, L = Longitudinal direction, T = Transverse direction, and S = Short Transverse Direction.

A 10kN motorized tensile (and compression) module supplied by Kammrath and Weiss, GmbH, Germany was used to elastically stress the specimens, Figure 3.15. The load was measured in a load cell, located at the rear side yoke of the module (see Figure 3.15). This load cell allowed force measurements from -10000 N to 10000 N for the particular tensile/compression module. The displacement (elongation) measurements were recorded by a differential transformer (“LVDT”), mounted parallel to the leadscrews. The tensile movement was activated using two parallel lead screws with one left, and one right pitch thread at either end. Adjustable bronze nuts in two opposing "yokes" bear these leadscrews, and applied the force evenly. A DC motor and two sets of worm gears applied the downgeared main shaft rotation. This resulted in a self-locking mechanism of high rigidity, where the experiment forces were all enclosed in the rectangular load frame. One of the advantages of this design is the fact that both yokes apply the movement equally to both sides of the specimen. The tensile module was controlled by the DDS controller/microprocessor supplied with the module. This controller can be operated independently or through a computer using DDS software. The microprocessor provided pre-selected displacement speed over a range of 0.1 μm/s to 20 μm/s.

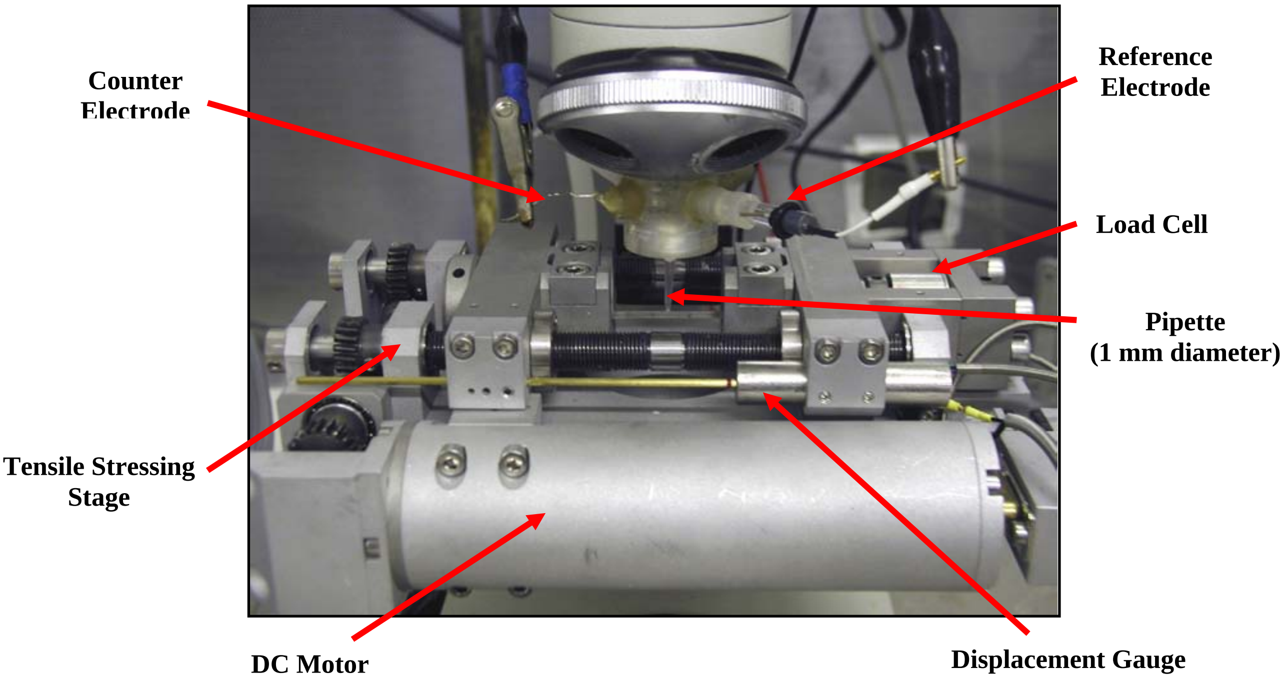

Figure 3.15 Local electrochemical (Capillary Cell) set up in conjunction with the tensile module. The stressing stage/module was mounted on the microscope stage which allowed easy movement of the sample in the 'z' direction. Stressing stage isolated from the microscope stage by PTFE sheet.

The most important factor while performing these experiments was to make sure that the specimen was completely isolated from the tensile stage, specially from the load cell. Any contact of the specimen with the stressing stage made it impossible to perform any electrochemical tests as the stage itself acted as a source of constant current. So, first the stressing stage was isolated from the microscope stage using a non-conductive PTFE sheet. The specimens were normally held by a metal grip in the stressing stage. These grips were made from Zircaloy and then heat treated for 12 hrs at 650˚C. This heat treatment formed a thick and non-conductive oxide layer on the surface of the grips. Use of these grips during the tests ensured complete isolation of the test specimen.

Before putting the specimen in the stressing stage, the load and elongation value of the set up was brought to zero using the microprocessor control. The thickness and the width of the specimens were measured carefully before mounting them in the stressing stage. The screws used for tightening the grips were also covered using PTFE tape to ensure electrical isolation of the specimen. Complete isolation of the specimen was checked repeatedly using a hand held voltmeter. Normally after tightening the screws on the specimen, load value showed a negative value. Load value was brought to zero using the stress stage controls. Based on the sample cross section, the desired load (in N) was calculated as a fraction of yield stress of AA2024-T351. For example, an AA2024-T351 specimen with a cross section of 12.5 mm^2 was calculated to need about 3280 N (i.e., $375 \times 12.5 \times 0.7$) of load for stressing to 70% of its yield stress (as yield stress of AA2024-T351 is 375 MPa). In this current study tests on AA2024-T351 specimens were carried out at a stress level of 45%, 70%, and 90% of its yield strength. Stress was assumed to be distributed uniformly through out the specimen in the elastic region.

Electrochemical tests of the unstressed specimen were performed at the areas slightly far from the middle of the specimen. Once the experiments were completed on the specimen in the unstressed condition, the specimen was stressed to the pre-calculated load. Displacement speed during the stressing was kept between 2-5 µm/s. The software simultaneously gave the load (N) vs. time (s) curve or load (N) vs. elongation (µm) curve. The tensile module was used in two ways for keeping the load constant at the desired level. After reaching to the pre-calculated load, the motor was stopped and hence the sample stayed at that particular load. However, there was also a 'constant load' option with the tensile module which allows the specimens to be kept at a particular load. Load was monitored as a function of time during the course of experiments. In few occasions a 40-50 N decrease in the load had been observed over a period of 3-4 hours. Any further decrease in the load was compensated by stressing the specimen again to the original value. Once the tests were completed, the specimen was brought back to zero load and taken out of the stressing module.

All experiments on AA2024-T351 to find out the effect of elastic stress were performed in naturally aerated 0.01 M NaCl at room temperature. Before the polarization, the open circuit potential (OCP) of the exposed area was monitored for 60-300 seconds. After the initial hold, anodic polarization was started at a negative potential of 50 mV (i.e., 50 mV in the cathodic domain) with respect to the OCP. Potentiodynamic scans were performed in similar fashion as it was described in Section 3.7.1 (i.e., at a scan rate of 1 mV/s).

As the potentiodynamic scans were not conclusive enough to find out the effect of low applied elastic stresses (i.e., 45% and 70% Y.S.) on the corrosion properties (corrosion and breakdown potentials, passive current densities etc.) of the AA2024-T351 specimens, effect of applied stress was further investigated using a potentiostatic polarization technique and calculating the charge passed within a defined time span. According to Faraday's Law, the higher the dissolution of the exposed material, the higher the amount of charge passed. During the potentiostatic tests, data was collected in the form of current (A) vs. time (s) through the software controlling the CHI600B potentiostat. Data collection frequency was set at 10 Hz. After the completion of the test, collected data was converted into text format and analysed by a commercial software named ‘KaleidaGraph (version 4.0)’. Current passed during the tests was converted to current density depending on the exposed area (~1.2 mm^2 in this case) and plotted as a function of time (s). As the charge in coulomb (C) is represented by the multiplication of current in ampere (A) with time in second (s), the KaleidaGraph software was used to integrate the current (A) vs. time (s) plot obtained from the potentiostatic test. The KaleidaGraph software was used to run a macro for calculating the indefinite integral, yielding a new curve. This macro found the incremental area under the curve, given the X-Y data points [in this case time (s) and current (A)] describing the curve. Integration of the current density (A/cm^2) vs. time (s) plot resulted in a new curve with charge density (C/cm^2) vs. time (s). Each point on this curve indicated the density of the total charge passed until that time during the experiment.

3.7.3 Micro-Capillary Electrochemical Cell Studies Under Applied Elastic/Plastic Stress Using Tensile Stage

This section describes the micro-capillary electrochemical cell (with an exposed area of 40 µm diameter) tests performed on the elastically/plastically stressed AA2024-T351 samples. Specimens were taken from the middle section of a 6 mm thick plate of AA2024-T351 and given the shape of a double notch flat tensile specimen with two semicircular notches at the middle by machining. The typical shape and dimension of such tensile specimen is shown in Figure 3.16. Load was applied perpendicular to the rolling direction of the plate. Sample preparation and the local electrochemical set up were similar to that of described in Section 3.7.2. Apart from the specimen shape, the main difference between these two sections is that, in this current section, a capillary diameter of 40 µm was used instead of 1 mm diameter pipette (as used in Section 3.7.2). As the same 10kN motorized tensile (and compression) module supplied by Kammrath and Weiss, GmbH, Germany was used in both cases to stress the specimens, the specimen mounting on the stressing stage and operating procedure were similar. The small exposure area of this technique allowed the possibility of performing a series of electrochemical tests as a function of stress on a particular notched specimen with a stress distribution (both elastic and plastic) around the notch.

A numerical simulation based on the finite element method was performed to calculate the surface stress on notched tensile AA2024-T351 specimens (schematic of such specimen is shown in Figure 3.16).[11] QUA4 elements composed of four nodes located at the four geometric corners of quadrangles were used in the meshing and the density of elements was chosen such that the size of an element was around 1 µm. The different equations and the conventions used in the mechanical analysis can be found elsewhere [312]. The matrix was assumed to behave like an isotropic elastic-plastic medium (E = 83 GPa and n = 0.33). The elastic-plastic material model used for the matrix was determined by fitting an experimental stress-strain curve (as described in Section 3.6.1) with the finite-element method model. The surface stress field was calculated under constant loading conditions. Stress distribution around the semicircular notch at the middle of the specimen varied depending on the applied global stress. The applied global

---

[11] Numerical analysis was performed by Vincent Vignal from LRRS, Université de Bourgogne, Dijon, France as a part of an International collaboration funded by the Royal Society, UK.

stress was chosen in such a way that it would give a fairly good distribution of elastic and plastic stresses around the notch. The idea behind the experimental plan was to place the micro-capillary (40 µm diameter) in elastically and plastically stressed areas and try to access the corrosion behaviour of different microstructural features as a function of applied stress. It was seen that an applied global stress of 200 MPa gave a good distribution of stresses over a comparatively large area in comparison to the 40 µm diameter area exposed during the micro-capillary electrochemical testing.

Naturally aerated 0.1 M NaCl solution at room temperature was used as an electrolyte during the experiments. Potentiodynamic scans were performed in the similar manner as already been described in Section 3.5 and potentiostatic polarizations were similar to that of described in Section 3.7.2.

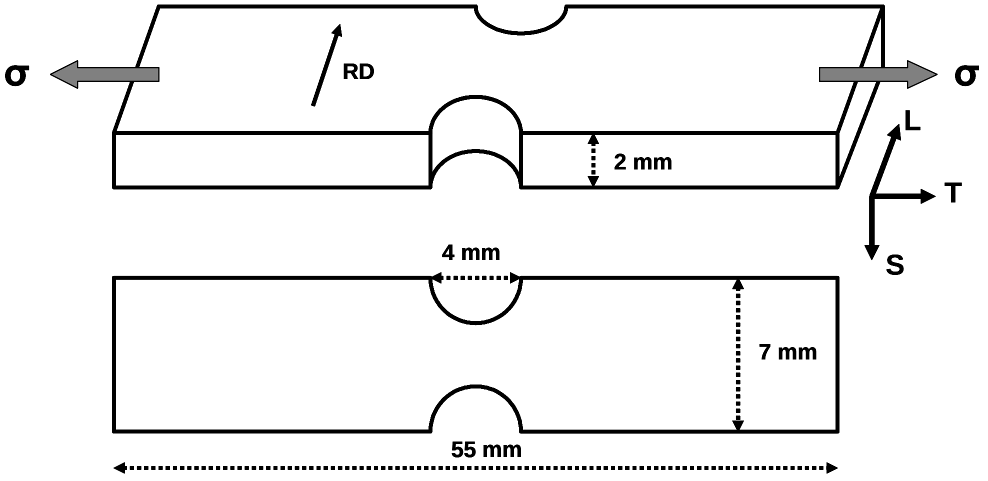

Figure 3.16 Schematic of a typical notched specimen used in the motorized tensile module in conjunction with the local capillary cell electrochemical tests. Load was applied perpendicular to the rolling direction. RD = Rolling Direction, L = Longitudinal direction, T = Transverse direction, and S = Short Transverse Direction.

3.8 X-Ray Synchrotron Tomography

3.8.1 Sample Preparation for the Synchrotron Studies

Aluminium alloy 2024 was tested in a sensitized temper during the current study in an unstressed condition as well as with the application of a tensile stress. The sensitized AA2024 temper was previously shown to simulate the electrochemical behaviour of the heat affected zone (HAZ) in the friction stir welded plate [313]. Specimens were made from the mid section of a 6 mm thick plate (Figure 3.17) which was heat treated at 250°C for two hours followed by water quenching. Synchrotron X-ray tomography experiments with this particular sensitized temper in unstressed condition is reported elsewhere in details [235, 288].

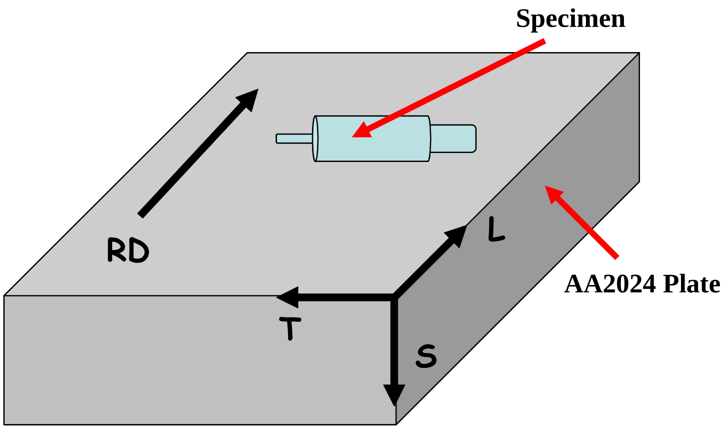

Figure 3.17 Machined specimens from the AA2024 rolled plate. RD = Rolling direction, L = Longitudinal, T = Transverse, and S = Short Transverse direction.

It can be seen from Figure 3.17 that the axis of the specimens was oriented perpendicular to the rolling direction of the aluminium alloy plate. As the synchrotron technique depends on the transmission of the X-ray beam through the specimens, the specimen size was dictated by the incident beam energy and several other parameters (i.e., X-ray scintillator efficiency, signal to noise ration etc.) of the beam line set up. Both unstressed and stressed samples were machined from the heat treated plate in the form a 500 µm diameter ‘matchstick’ cylindrical specimen and ‘dog-bone’ type tensile specimen with gauge diameter of 500 µm respectively (Figure 3.18). The unstressed specimens were machined first to 3 mm rods and then the upper 2 mm was turned to 500 µm diameter pins. The stressed specimens were machined to 3 mm rods first and then given the dog-bone shape with a gauge length of about 2 mm and gauge diameter of 500 µm.

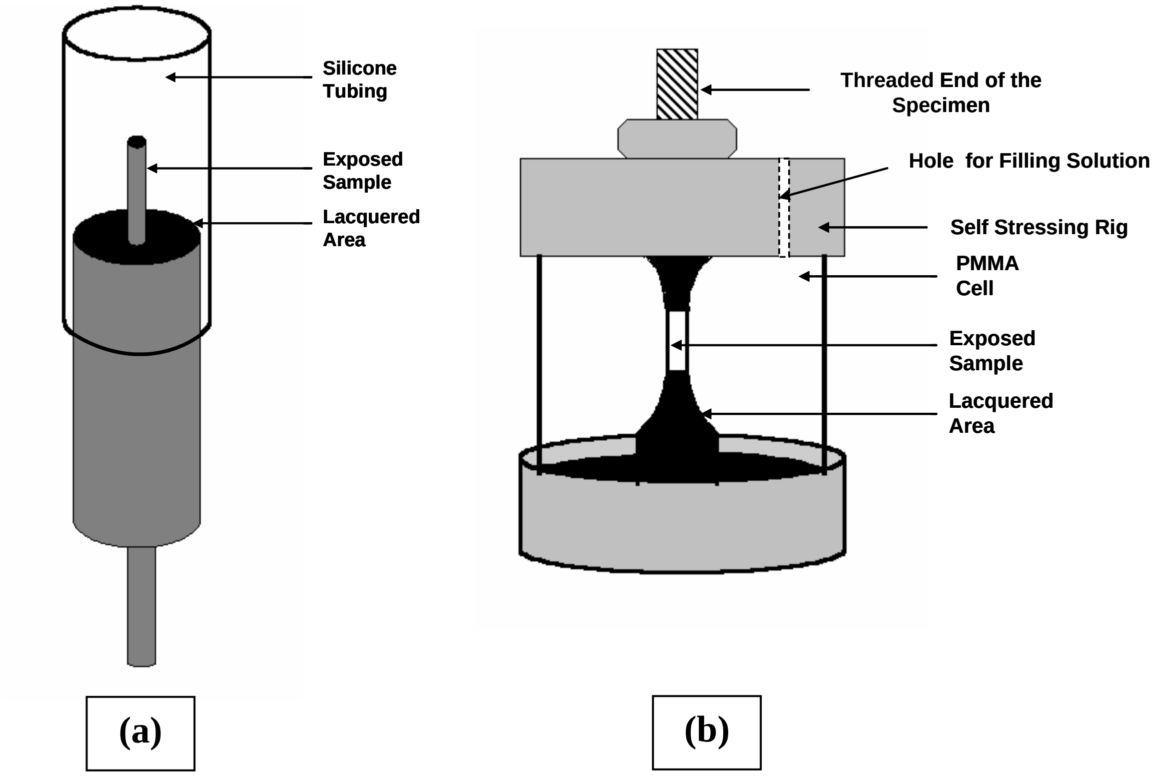

Figure 3.18 Specimens for X-ray synchrotron tomographic study with specially adapted environmental cell around them, (a) Specimen in unstressed condition, (b) Pre-stressed specimen within the self stressing rig.

All the samples were tested in naturally aerated 0.6 M NaCl solution using a specially adapted environmental cell (see Figure 3.18a and b). As shown in the figure, all samples (both unstressed and stressed specimens) were lacquered with Stopping Off Lacquer to avoid any unwanted material exposure or crevicing. Silicone tubing and PMMA polymer was used around the unstressed and stressed sample respectively to form the environmental cell. Dog bone tensile specimens with 500 µm diameters were stressed to 70% and 90% of the yield stress (yield stress of sensitized temper AA2024 was determined to be about 375 MPa from the average of two repeat experiments) prior to the experiments using a self-stressing rig as shown in Figure 3.19. In all cases stress was applied perpendicular to the rolling direction of the aluminium plate.

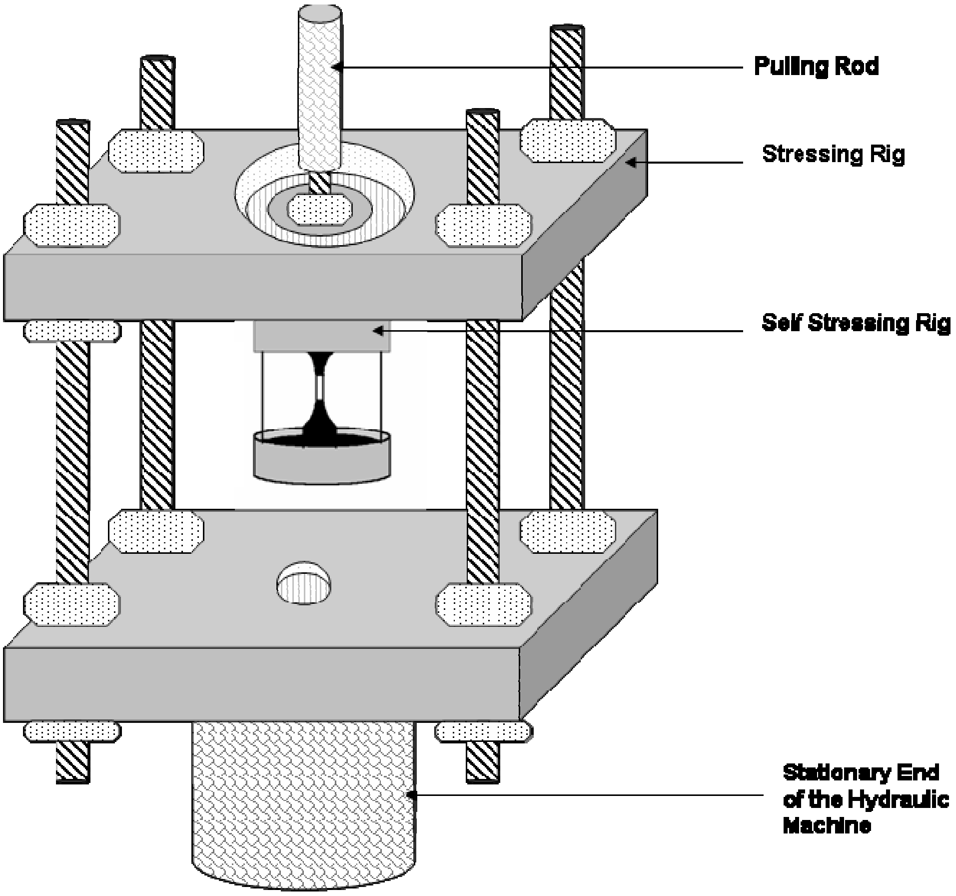

Figure 3.19 Pre-stressing the sample using a combination of stressing rig and a servo hydraulic machine.

An ESH Servo-Hydraulic low flow 200kN fatigue testing machine was used to stress the samples. Both ends of the dog bone sample were threaded. One threaded end of the specimen was screwed in the bottom mild steel adapter. The other end of the threaded specimen was passed through a hole in the upper mild steel adapter and was tightened using a nut against it (see Figure 3.18b).

All steel surfaces were coated with stop off lacquer. The PMMA cell which was kept between the two adapters acted as the environmental cell and kept the adaptors separated. Another hole in the top adapter was made to fill the cell with test solution prior to experiments on the synchrotron beam line. The stressing rig was made of two square plates of steel and was separated at a constant distance using four firm threaded rods and nuts (see Figure 3.19). The upper plate of the rig had a hole which was bigger than the diameter of the specimen but smaller than the diameter of the steel adapters. The bottom plate of the stressing rig was attached to the stationary end of the hydraulic machine. The threaded end of the sample went through the hole in the top plate and attached to the pulling rod of the hydraulic machine. When the upper face of the top steel adapter touched the lower face of the top plate of the rig, machine was set to zero load. The hydraulic machine was then used to pull the sample to a predetermined value. Once the predetermined value is reached, the small nut in the treaded sample was tightened against the top face of the top steel adapter to keep the tensile sample in that specified load. To check the compatibility of the polymer cell at high load, compression tests were performed for a period of three days at a load equivalent of 90% YS of the sample using the same hydraulic machine. It was observed that the PMMA cell was able to retain the equivalent load of 90% Y.S. without any relaxation.

3.8.2 Synchrotron Experiments in the Beam Line and the Reconstruction Procedure

In situ[12] Synchrotron tomographic experiments were performed on the Materials Science beam line X04SA at the Swiss Light Source (SLS), Paul Scherrer Institute, in Switzerland [262] to quantify the effect of applied stress on the propagation of localized corrosion (IGC) as a function of time. Tomographic scans were performed on unstressed and stressed AA2024 (sensitized temper) specimens exposed to 0.6 M NaCl solution at room temperature at open circuit. Times for each tomographic scans were between 40 and 60 min in duration. A sequence of tomographic scans was then performed on each specimen at certain interval during the exposure up to a maximum of two days. As described earlier (see Figure 3.18a and b), the environmental cell around the specimens were filled, at the beam line, with solution before the start of the first scan of respective specimens. Deionized water was added to the environmental cell whenever necessary during the exposure to compensate the solution loss due to evaporation.

The energy of the monochromatic X-ray beam was set to 17.5 keV. The distance between the sample and the CCD camera detector was 30 mm (Figure 3.20). The X-ray detector system optics were set up so that the radiographic images were magnified by 40x between the scintillator and the CCD camera, which was set to acquire 1024 × 1024 pixels of data. During the 180° rotation of the sample (using a 0.3 s exposure/projection), a series of 1023 radiographs (2D) were taken. The recorded radiographs were reconstructed to 3D volumes using filtered back projection algorithm [314]. The data

---

[12] During the in situ experiments, specimens within the environmental cell (i.e., specimens immersed in the corrosive solution) were placed in the synchrotron beam line for tomographic scan. This technique allowed real time monitoring of the corrosion process.

were obtained in the form of a three dimensional array of voxels (with a theoretical isotropic voxel resolution of 0.7 μm), for which the grey level of each voxel describes the calculated X-ray attenuation at that position [290]. A photo of the experimental set up is shown in Figure 3.20.[13] All the scans were in situ (i.e., with the solution inside the cell while scanning) and were recorded as a function of time. Further details about the experimental set up at SLS could be found elsewhere [288, 289].

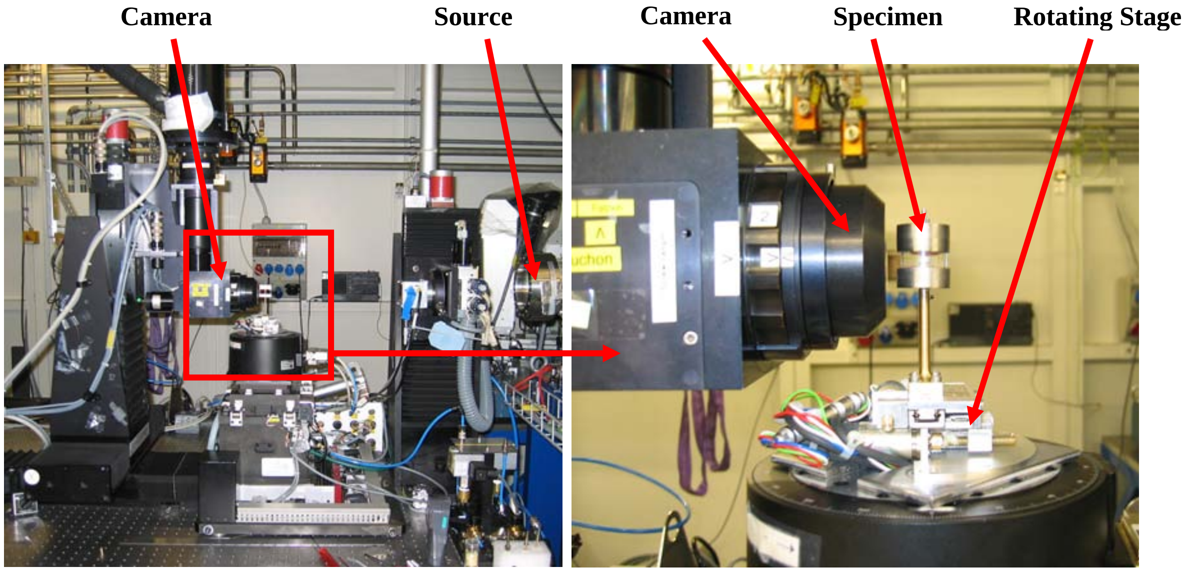

Figure 3.20 Experimental set-up for X-ray synchrotron tomographic experiment. X-ray synchrotron beam comes from the source and goes through the specimen. Transmitted beam is recorded using the CCD camera. Specimen is being rotated using the stage during the course of experiment.

---

[13] Basics of the X-ray synchrotron tomography and the reconstruction procedure are described in Section 2.4 of Chapter 2.

3.8.3 3D Visualization and Analysis of the Tomographic Data

Visualization and 3D analysis of the tomography data from the synchrotron experiments were performed using the commercial 3D visualization and modelling software ‘Amira’. Using this software, two dimensional tomographs were combined together to provide a 3D representation of the corrosion attack morphology and its interaction with the alloy microstructure.

Reconstructed raw data (in the “rec.DMP” format) were directly loaded into the software as a stack of 2D slices. Various data processing modules (e.g., contrast control) helped in simple and efficient manipulation of the image. The image segment editor[14] of this particular software (i.e., ‘Amira’) was used to label voxels corresponding to the alloy matrix, intermetallic particles and corrosion based the differences in their contrast values. The labelled regions of each specimen were then represented in three dimensions (3D) as triangular surface grids suitable for numerical analysis and simulations. Different features (e.g., corrosion attacks, alloy matrix) were labelled in different colours and the specimen matrix material has been rendered translucent in order to observe the morphology of corrosion attacks within the interior of the specimen. With the input of voxel sizes in 3D space (i.e., 0.7 μm in x, y, and z axis in this case), quantitative analysis of the labelled regions were performed.

Volume of both the corrosion attacks and the samples exposed during the tomographic scans were calculated using the software. Based on these calculations, growth rate of corrosion attacks as a function of exposure time were expressed as volume of metal loss as a percentage of specimen volume (see Chapter 7).

---

[14] Segmentation is a process of dividing an image data into different segments for 3D model reconstruction.

4 EFFECT OF SURFACE TREATMENT AND ITS BENEFICIAL EFFECT ON THE CORROSION PROPERTIES OF AA2024-T351

High strength aluminium alloy 2024-T351 is susceptible to localized corrosion in the forms of pitting and intergranular corrosion, which can be potential sites for initiation of cracks and thereby could result in catastrophic failure. Two predominant categories of second-phase intermetallic particles have been identified in AA2024-T3: elongated or irregular shaped Al-Cu-Fe-Mn containing particles [$Al_6(CuFeMn)$ or with other stoichiometric relationships; in short they will be termed as “Fe-Mn” particle throughout this study] which are generally believed to act as cathode during the corrosion process [7-9, 11, 175, 186, 187, 191] and ‘S’ (Al_2CuMg) phase intermetallic particles which show initial anodic behaviour during the corrosion process. However, dealloying of ‘S’ phase particles can then lead to Cu enrichment on the particles and make them cathodically active. Hence, ‘S’ phase particles are thought to be the key contributor for the poor corrosion resistance of AA2024 [8, 12, 14, 37, 40, 43, 46, 174, 185, 198].

The key purpose of this study is to examine the effectiveness of a surface treatment technique in removing deleterious ‘S’ phase particles from the surface and thereby improving the corrosion properties of AA2024-T351. The effects of ‘S’ phase particle removal on the initiation of localized corrosion in AA2024-T351 have been investigated using several electrochemical techniques during this present study.

4.1 Microstructural Characterization of AA2024-T351

Scanning Electron Microscopic (SEM) analysis of polished AA2024-T351 was performed in both high low and high magnification to reveal the general microstructure as well as the morphology of the individual intermetallic particles. EDS spectrums were use to quantify the composition of each types of intermetallic particles and the base metal matrix. Figure 4.1(a) shows the general microstructure of AA2024-T351 base metal surface as revealed by low magnification SEM micrographs. The presence of a large number of constituent intermetallic particles can easily be seen from the micrographs. Sometimes the intermetallic particles are formed as clusters and after cold rolling they break up and often align parallel to the rolling direction. Figure 4.1(a) also shows the presence of some pre-existing hole or pores in the sample. Presence of such holes/pores in the AA2024-T351 had also been confirmed using synchrotron studies and will be discussed later in Chapter 7. EDS analysis showed that the matrix of AA2024-T351 mainly consists of ~ 93 wt% Al, ~ 1.2 wt% Mg, ~ 4 wt% Cu with small amount of impurity element like Fe, Mn and Si.

4.1.1 The Intermetallic Particles

Two predominant categories of coarse intermetallic particles have been identified in the microstructure as shown in Figure 4.1(b) and Figure 4.1(c). The first type is irregular in shape and in the size range of 10-20 µm containing mainly Fe-Mn-Cu-Al (Figure 4.1b). In very few occasions these Fe-containing intermetallic particles are found to contain Si.

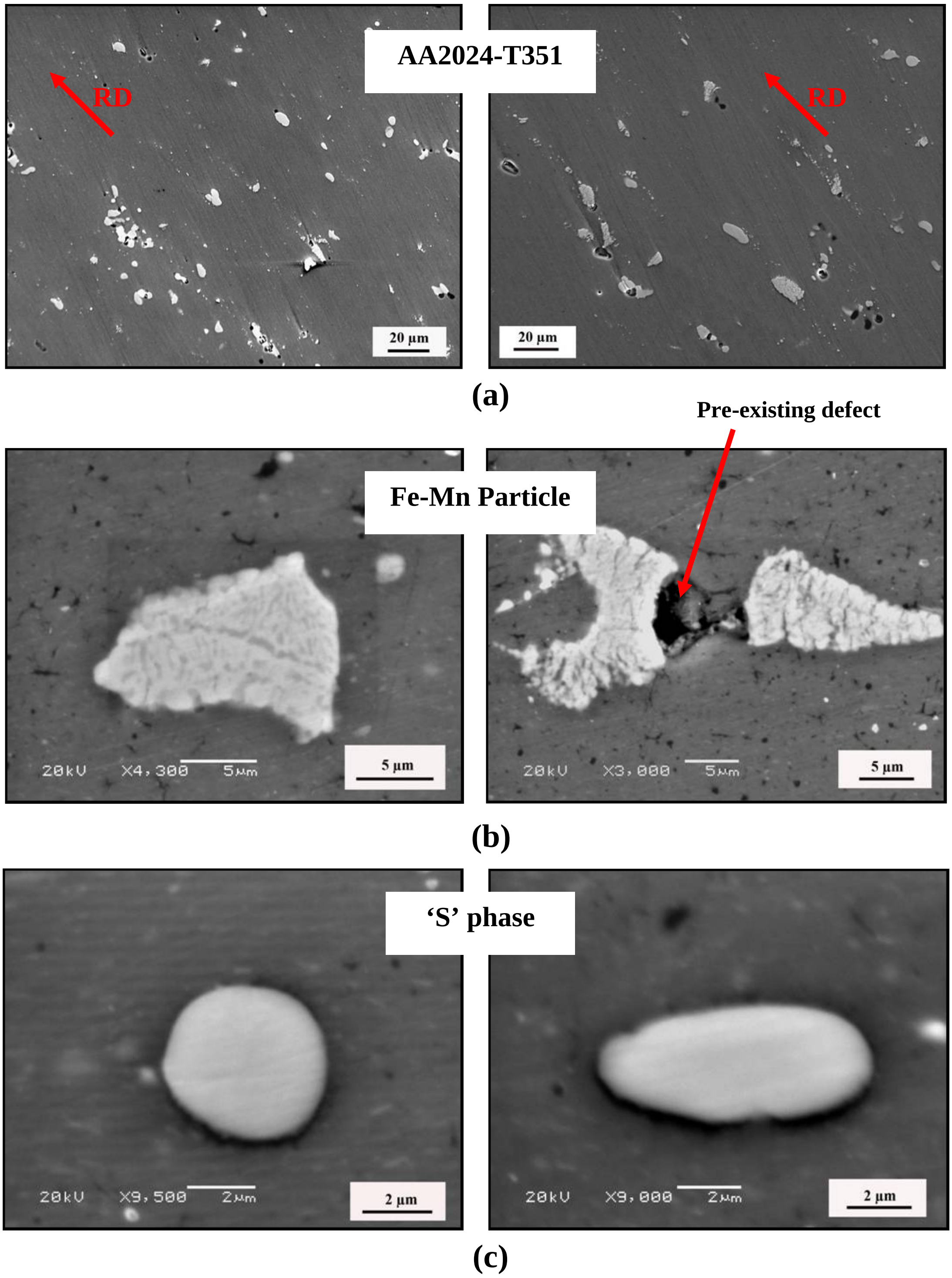

Figure 4.1 SEM micrographs of (a) As received 2024-T351 samples (RD = Rolling Direction). Some pre existing holes (from solidification stage) can be seen in the sample surface. (b) Typical Fe-Mn particles showing a pre-existing defect/crevice at the edge. (c) 'S' phase particles showing typical round and elongated shapes.

These particles are sometimes found to be broken into fragments during the subsequent thermo-mechanical treatment as they are harder than the matrix. This is consistent with the findings of others [7, 8, 81]. Pre-existing defects/crevices at the edge of Fe-containing particles are also found in several occasions (e.g. Figure 4.1b; further SEM and AFM analysis of such pre-existing defects can be found in Chapter 6) which is consistent with the observations of other researcher [235]. By comparison, the second types of coarse intermetallic particles containing Al-Cu-Mg are rounded and smooth in appearance within the size range of 2-5 µm (Figure 4.1c,). In a few cases these Al-Cu-Mg particles are found to be in an elongated shape and as large as ~ 10 µm in size. A small number of rounded and smooth particles are seen to contain Al and Cu. However, the numbers of Fe-containing particles having Si and Al-Cu particles are insignificant compared to the Fe-Mn-Cu-Al particles or Al-Cu-Mg particles. So, this study will primarily be focused on Fe-Mn-Cu-Al and Al-Cu-Mg intermetallic particles. Typical examples of EDS spectra of different types of intermetallic particles are shown in Figure 4.2. Compositional analysis of the two predominant types of intermetallic particles is shown in Table 4.1. Forty different particles of each type (ten particles each from four different AA2024-T351 samples) were analysed and the elemental compositional mean with their standard deviation were calculated. Table 4.1 shows the weight and atomic percentage of each element in different intermetallics.

The Al-Cu-Mg particles in AA2024 have been reported as Al_2CuMg or ‘S’ phase by several authors [5-9, 11, 19, 43-45, 70, 76, 80, 174, 198, 204, 211, 315]. It can clearly be seen from Table 4.1 that Al-Cu-Mg particles of this study closely follow the stoichiometric composition of Al_2CuMg and hence can be assigned as ‘S’ phase. As stated earlier, Al-Cu particles are less often observed in AA2024 compared to ‘S’ phase particles.

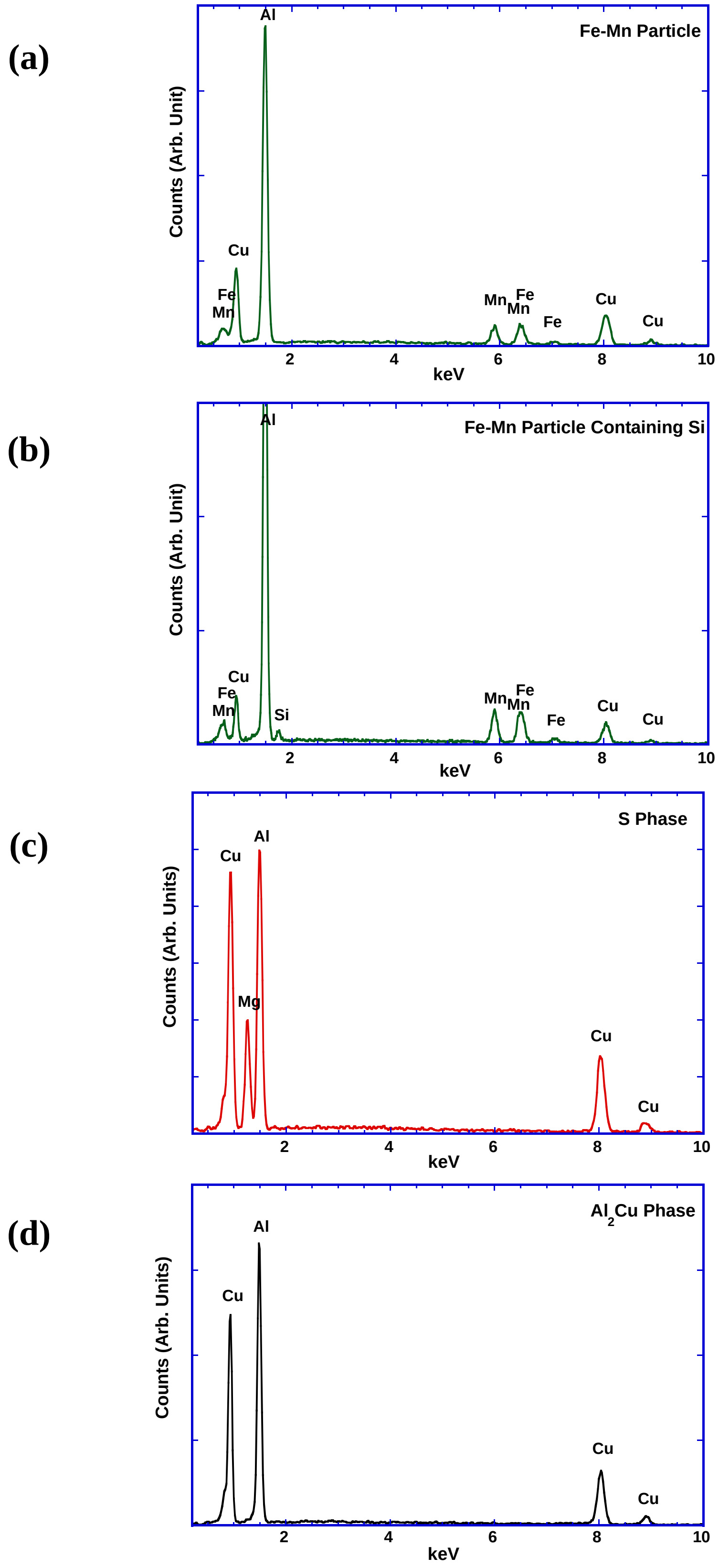

Figure 4.2 EDS spectrum of (a) typical Fe-Mn particle, (b) Fe-Mn particle containing Si, (c) 'S' phase particle (Al_2CuMg) and (d) θ phase (Al_2Cu) present in AA2024-T351. Only very few Fe-Mn particles contain Si.

Table 4.1 Composition (Weight and Atomic % ± Standard Deviation) of intermetallic particles in AA2024-T351

Element	Al		Cu		Mg		Fe		Mn	
	Wt.%	**At.%**	**Wt.%**	**At.%**	**Wt.%**	**At.%**	**Wt.%**	**At.%**	**Wt.%**	**At.%**
'S' phase	41.3 ± 3.5	54 ± 3.5	44 ± 3.7	24.7 ± 2.8	14.5 ± 2	21 ± 2.7	-	-	-	-
Fe-Mn Particle	55.6 ± 3.3	73.6 ± 2.4	27.9 ± 5.5	15.8 ± 3.4	-	-	7.8 ± 1.2	5 ± 0.9	8.8 ± 3.3	5.7 ± 2

In this present study the Al-Cu particles are found to consist of Al (wt% ~ 48.4±2, at% ~ 68.8±1.8) and Cu (wt% ~ 51.6±2, at% ~ 31.2±1.8). So, from the stoichiometric relationship the Al-Cu particles could be assigned as Al_2Cu and is consistent with the findings of other researchers [75]. These Al_2Cu particles are small, rounded (1-2 µm) and generally found as isolated individual particles.

However, the Fe-containing intermetallic particles from this present study seem to follow a stoichiometric relationship close to $Al_{15}Cu_3(Fe,Mn)$. Several compositions of Fe-containing intermetallic particles have been reported in the literature, $Al_6(CuFeMn)$ [9, 11], Cu_2AlFe_7 [9, 73, 204], $Al_7Cu_2(Fe,Mn)$ [76], $(Fe,Mn)_xSi(Al,Cu)_y$ [75, 78]. A very few Fe-containing intermetallic particles in this current study have been found to contain significant amounts of Si. Only one particle (among the 40 Fe-containing particles analyzed) showed the presence of ~2 wt% of Si. So, the current study emphasize the fact as pointed out by other researchers [7, 75] that the Fe-containing intermetallic particles in AA2024 may not always possess a particular and definite stoichiometric relationship. Hence the Fe-rich intermetallic particles will be referred as Fe-Mn particles/phase in this current study.

Figure 4.3 shows the summary of the compositional analysis of Fe-Mn particles and ‘S’ phase particles. Standard deviations of the weight percentages of each element are shown with the error bar in the bar chart. It is interesting to note that iron content (wt% 7.8 ± 1.2) of the Fe-Mn particles show the minimum standard deviation compared to its manganese (wt% 8.8 ± 3.3) and copper content (wt% 27.9 ± 5.5). Relatively high standard deviation in the copper content indicates that some Fe-Mn particles contain more copper than the others.

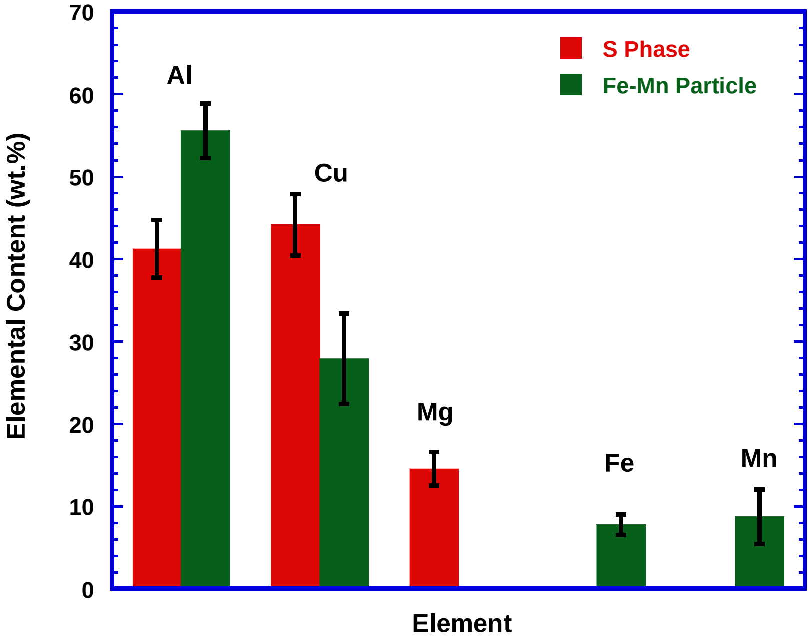

Figure 4.3 Compositional analysis of Fe-Mn particles and ‘S’ phase particles in AA2024-T351 as determined from EDS spectrums. Standard deviations of the elements are calculated from forty particles of each type and shown as error bar in the graph. Fe-Mn particles show relatively large variation in copper content.

4.2 Microstructure of AA2024-T351 After Surface Treatment

AA2024-T351 samples were treated to remove the ‘S’ phase particles from the surface after the samples were polished to one micron surface finish. The surface treatment involves an alkaline etch followed by desmutting in nitric acid containing chloride ions. Details of the surface treatment procedure have already been described in Chapter 3 (Experimental Procedure). Figure 4.4, Figure 4.5, and Figure 4.6 show the appearance of the AA2024-T351 matrix after different surface treatment as revealed by the SEM micrographic analysis.

Figure 4.4 shows the AA2024-T351 matrix after etching with NaOH and then desmutted in HNO_3 without chloride ions. It can easily been seen from the figure that both Fe-Mn particles and ‘S’ phase particles are still present in the microstructure. In some cases the irregular shaped Fe-Mn particles are found to be attacked at the edges [Figure 4.4(c) and (d)]. Round shaped and smooth ‘S’ phase particles do not change their appearance after the surface treatment and remain unattacked. However, after etching and desmutting, the submicron sized dispersoids and precipitates become visible in the matrix.

Figure 4.5 shows the SEM micrographs of the AA2024-T351 surface after the sample was treated in the presence of 10 mM $CeCl_3$ in the nitric acid desmut bath. It has to be noted that in this case the sample was treated in the same way as it was done for the sample shown in Figure 4.4, except an extra addition of 10 mM $CeCl_3$ in the nitric acid desmut bath of the former. A significant number of particles have disappeared from the matrix [Figure 4.5 (a) and (b)]. Dispersoids become visible in the matrix after the treatment as seen before (Figure 4.4). All the ‘S’ phase particles in the matrix were removed after the surface treatment with 10 mM $CeCl_3$ and holes of the shape of the ‘S’ phase particle in the matrix can easily be seen from the Figure 4.5 (a) and (b). Figure 4.5 (c) shows the high magnification micrograph of the alloy surface with holes which results from the removal of ‘S’ phase particles. EDS analysis did not find any trace of ‘S’ phase particles remaining in the matrix after the surface treatment. Most of the Fe-Mn particles were partially attacked [Figure 4.5(d) and (e)] whereas some remained unattacked (Figure 4.5b).

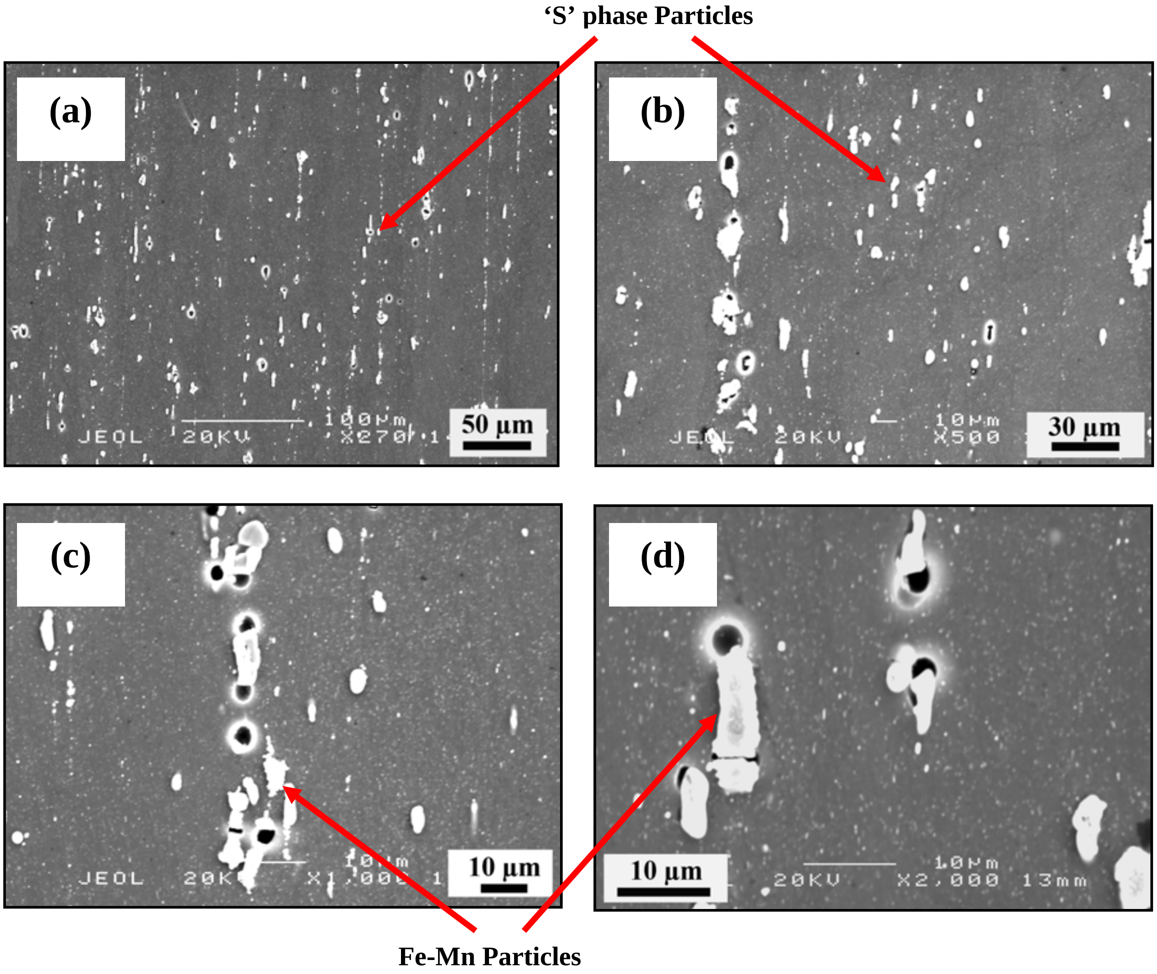

Figure 4.4 SEM images of the AA2024-T351 surface etched with NaOH and then desmutted in HNO_3 without chloride ion. (a)-(b) AA2024-T351 surface after the etching and desmutting treatment, (c)-(d) Partial dissolution of Fe-Mn particles can be seen in these images. ‘S’ phases remain unattacked after the surface treatment. Due to the etching of the surface, dispersoids in the alloy matrix become visible.

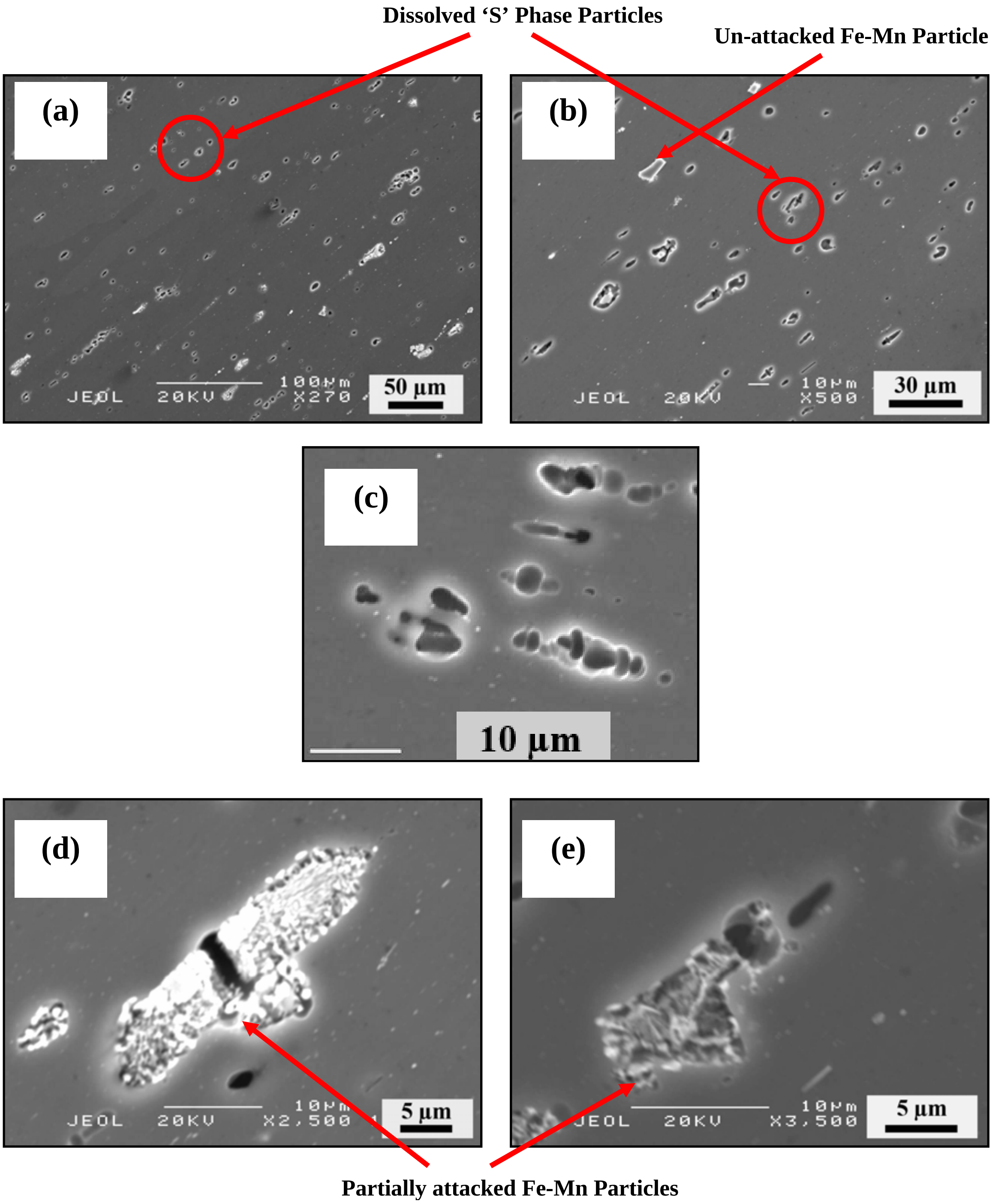

Figure 4.5 SEM images of the AA2024-T351 surface after alkaline etching followed by desmutting in nitric acid containing 10 mM $CeCl_3$. (a)-(b) Low magnification micrographs showing the presence of small rounded holes on the alloy surface resulting from the dissolution of ‘S’ phase particles, (c) High magnification micrograph showing holes due to the removal of ‘S’ phase particles, (d)-(e) Partially attacked Fe-Mn particles.

In order to distinguish the effect of cerium ions and chloride ions in removing the ‘S’ phase particles, another set of experiments were performed with the addition of 30 mM NaCl in the desmut bath. Addition of 30 mM of NaCl in the nitric desmut bath removed all the ‘S’ phase particles [Figure 4.6 (a) and (b)] from the matrix as it was seen in Figure 4.5. As before, most of the Fe-Mn particles are found to be attacked [Figure 4.6 (c) and (d)].

Dissolved ‘S’ Phase Particles

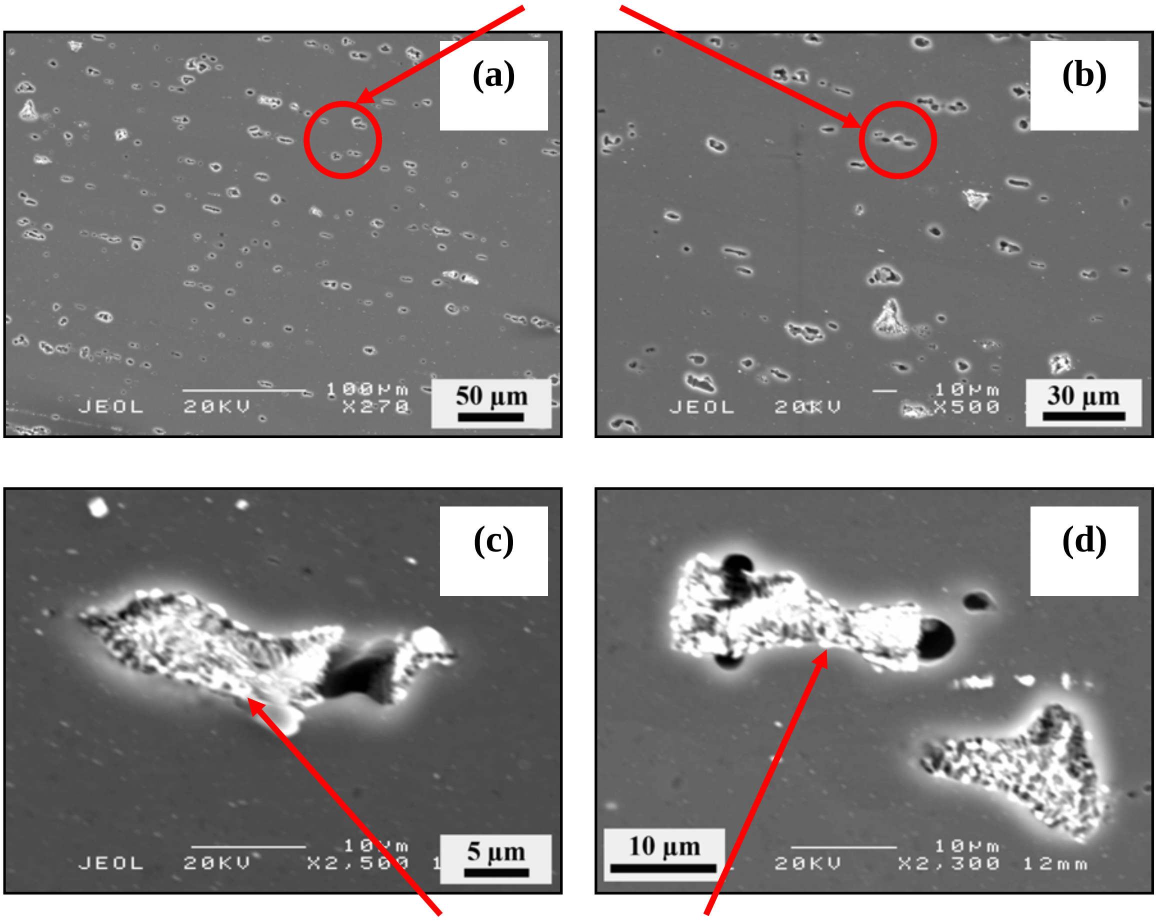

Partially attacked Fe-Mn Particles

Figure 4.6 SEM images of the AA2024-T3 surface showing the effect of the addition of 30 mM NaCl in the desmut bath on ‘S’ phase particle removal. (a)-(b) Low magnification micrographs showing the presence of small rounded holes on the alloy surface resulting from the dissolution of ‘S’ phase particles, (c)-(d) Partially attacked Fe-Mn particles.

Comparing Figure 4.5 and Figure 4.6, it can be concluded that the presence of chloride ions and not necessarily cerium in the nitric desmut bath is critical for removing the ‘S’ phase particles from the AA2024-T351 matrix. However, throughout the subsequent electrochemical experiments in this current study 10 mM $CeCl_3$ (instead of 30 mM NaCl) was used in the desmut bath to remove the ‘S’ phase particles from the AA2024-T351 matrix.

Profilometry was used (Figure 4.7) on the sample treated with 10 mM $CeCl_3$ to find out the extent of matrix dissolution during the whole surface treatment procedure. Part of the sample was covered with ‘stop-off’ lacquer prior to the surface treatment and then the sample was exposed to the surface treatment. After the treatment, the lacquer was removed and profilometry was conducted across the interface (i.e., lacquered vs. not lacquered surfaces). The left hand side of the Figure 4.7 represents the line profile on the untreated surface, whereas the right hand side of the same figure shows the profile after surface treatment. It can be seen from Figure 4.7 that the matrix was dissolved by approximately 900 nm to 1 µm during the treatment. Peaks on the line scan in the positive direction relative to the mean probably represent the partially attacked (or unattacked) Fe-Mn particles, whereas transients in the negative direction are probably due to the completely removed ‘S’ phase particles which leave behind holes on the surface of AA2024-T351.

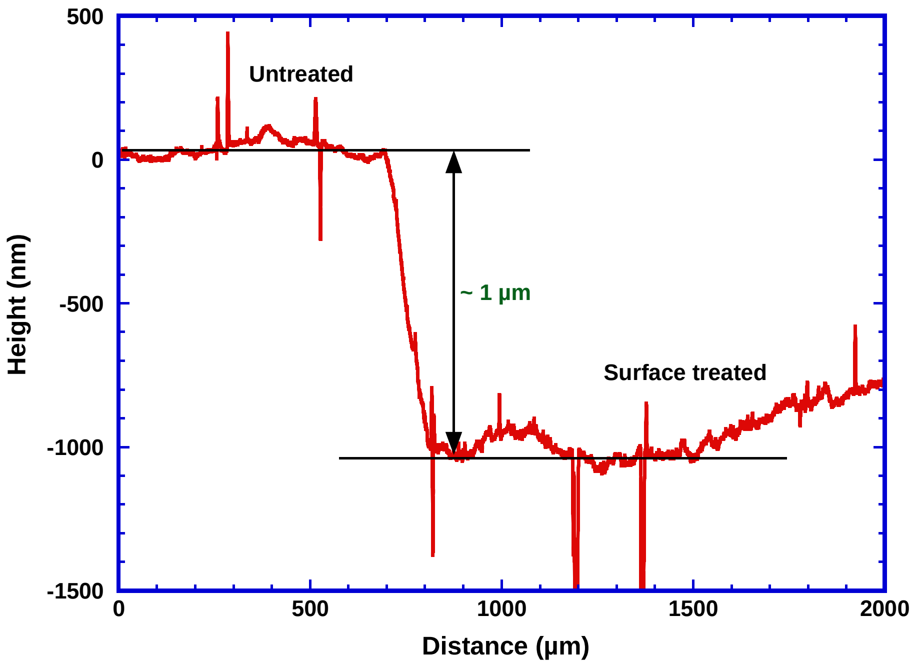

Figure 4.7 Line profilometric study (using Stylet Profilometer DekTak® 6M) showing the depth of attack during the surface treatment as measured between the untreated and treated part of the same AA2024-T351 sample. Surface treatment resulted in almost one micron depth of alloy dissolution.

4.3 Anodic Potentiodynamic Polarization Measurements

4.3.1 In Naturally Aerated 10 mM NaCl Solution

Anodic potentiodynamic polarization scans were performed in naturally aerated 10 mM NaCl solution at room temperature on as received and different surface treated samples as shown in Figure 4.8. Scans were performed with a rate of 1 mV/s and on freshly polished exposed sample area of 1.2 cm^2 of one micron surface finish. Apart from the etched and surface treated samples, scans were also performed on the samples only dipped in HNO_3 for 30s after polishing. These scans are represented with the blue colour.

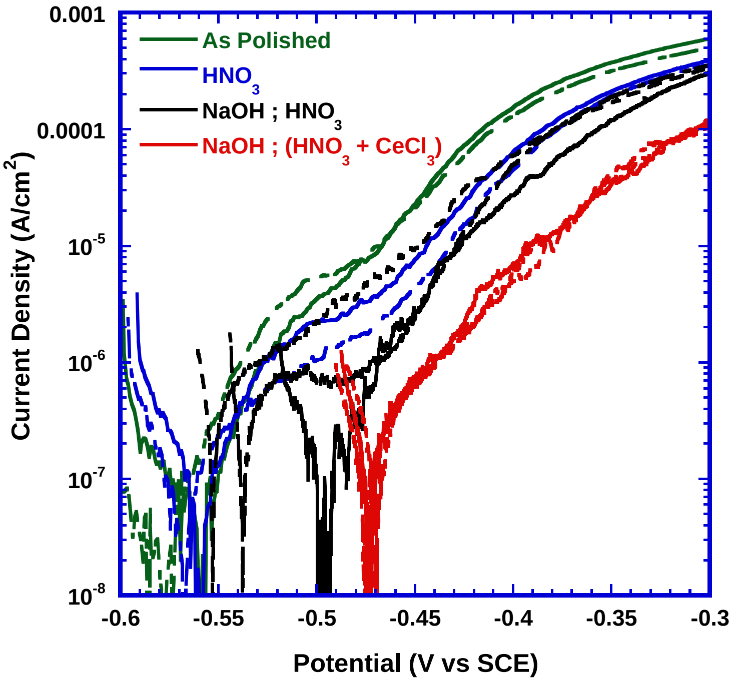

Figure 4.8 Anodic polarization scans of AA2024-T351 in naturally aerated 10 mM NaCl (scan rate = 1 mV/s) showing the effect of surface treatment. Anodic reactivity of the 'S' phase removed samples (with $CeCl_3$ addition) are lower than the untreated samples.

It is can be seen from Figure 4.8 that most of these scans do not show any definite passive region or any sharp breakdown potential. So, an arbitrary current density (10 µA/cm^2) is chosen as a representative breakdown current density and the potential at this current density is referred as the breakdown potential for each scan. It can clearly be seen from the figure that the samples without 'S' phase particles show lower anodic reactivity compared to the samples with 'S' phase particles. Breakdown potentials for the NaOH ; (HNO_3 + $CeCl_3$) treated samples (i.e., without 'S' phase particles) are higher compared to the as polished and NaOH ; HNO_3 treated samples. It is evident that scans for the NaOH ; (HNO_3 + $CeCl_3$) treated samples (without 'S' phase particles) are very reproducible whereas NaOH ; HNO_3 treated samples (with 'S' phase particles) show greater scatter. Increase in the breakdown potential after the removal of 'S' phase particles from the matrix [i.e., NaOH ; (HNO_3 + $CeCl_3$) treated samples] emphasizes the effectiveness of this particular surface treatment and the deleterious effect of the 'S' phase particles.

Another set of experiments on different surface treated samples were done with 1200 grit surface finish (results not shown). Similar trends have been observed with 1200 grit surface finish as it is found in Figure 4.8 (one micron surface finish).

4.3.2 In Deaerated 10 mM NaCl

Figure 4.9 shows the anodic polarization scans of AA2024-T351 samples with different treatments in deaerated 10 mM NaCl. Scan rate (1 mV/s), exposed area (1.2 cm^2) and surface finish (freshly polished to one micron). These experiments were similar to the experiments performed in aerated condition. Details of checking extent of deaeration prior to each experiment have already been discussed in the experimental procedure section (Chapter 3). A definite passive range and breakdown potential can clearly been identified after deaerating the solution for all samples. The effect of oxygen on the open circuit potential can be seen by comparing Figure 4.9 with Figure 4.8. The absence of oxygen decreases the cathodic reactivity (which is predominantly oxygen reduction in this case) and hence decreases the OCP. The samples treated with 10 mM $CeCl_3$ seem to indicate higher breakdown potential than other samples with different treatments. Passive current densities for both NaOH ; HNO_3 and NaOH ; (HNO_3 + $CeCl_3$) treated samples are higher than the as polished and polished + HNO_3 treated samples. The exact reason for the higher passive current densities after the NaOH etching is not clearly understood as yet. However, the process resulting in visible dispersoids and precipitates after the surface treatment (Figure 4.4 and Figure 4.5) could play a role in increasing the passive current densities.

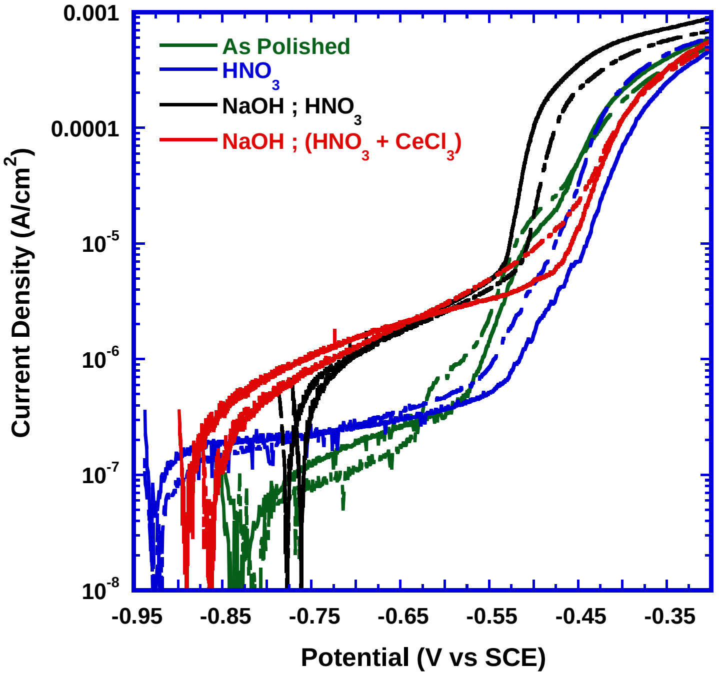

Figure 4.9 Anodic polarization scans of AA2024-T351 in deaerated 10 mM NaCl (scan rate = 1 mV/s) showing the effect of surface treatment.

4.4 Cathodic Potentiodynamic Polarization Measurements

Cathodic reactivity plays an important role in the corrosion of aluminium alloys. The predominant cathodic reaction for corrosion of aluminium alloys is oxygen reduction which leads to the increase in local alkalinity. The passive oxide film responsible for protecting the aluminium alloy from corrosion can dissolve in both high and low pH. As every anodic reaction during corrosion should be supported by equivalent cathodic reaction, in many cases corrosion can be limited by the supply of cathodic current. High cathodic reactivity makes the corrosion process faster. This section will summarize the results from different cathodic polarization scans as performed on the surface treated samples to find the effect of 'S' phase particle removal by $CeCl_3$ treatment on the cathodic reactivity of the samples.

Figure 4.10 shows the cathodic polarization scans of samples in naturally aerated 10 mM NaCl solution while desmutted with HNO_3 and with HNO_3 + 10 mM $CeCl_3$ after etching in NaOH. Initial cathodic reactivity of the $CeCl_3$ treated samples (without 'S' phase particles) are lower than the cathodic reactivity of the samples desmutted only with HNO_3 (with 'S' phase particles). Sample desmutted with only HNO_3 shows a stable oxygen reduction plateau from ~ - 600 mV to ~ -1050 mV vs. SCE at a cathodic current density of ~ 7×10^{-6} A/cm^2. Though the initial cathodic current of the HNO_3 + 10 mM $CeCl_3$ samples are less compared to the HNO_3 treated samples, it eventually reached an oxygen plateau, although shorter, at the same cathodic current density. Even after the oxygen plateau, samples without 'S' phase particles show lower cathodic reactivity than the samples with 'S' phase particles.

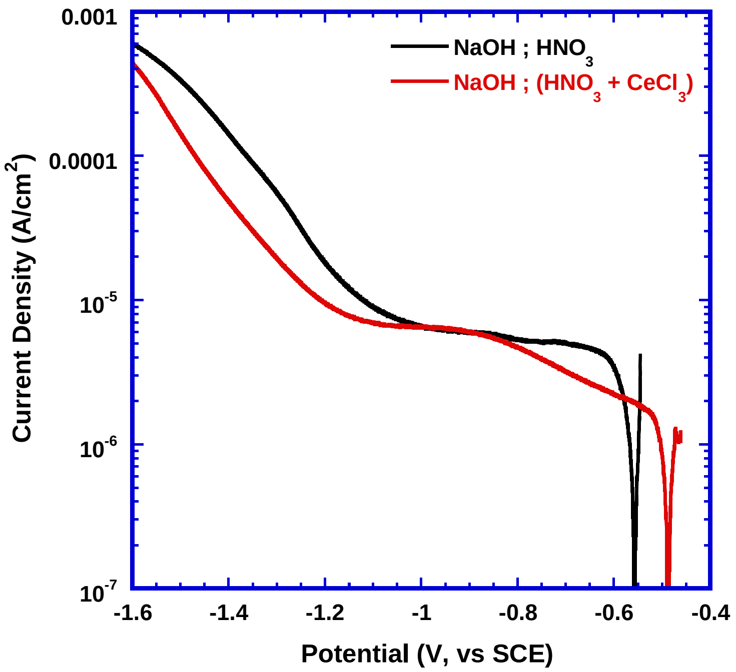

Figure 4.10 Cathodic polarization scans of AA2024-T351 in naturally aerated 10 mM NaCl (scan rate = 1 mV/s). 'S' phase particles removed samples (with $CeCl_3$ addition) show lower cathodic reactivity than the samples having 'S' phase particles.

However, the change in local alkalinity due to oxygen reduction reaction during the cathodic polarization scans should also be considered while comparing the sample with and without ‘S’ phase particles. The increase in local alkalinity dissolves the passive film and thereby expose bare alloy surface which also might affect the cathodic current densities. This process makes it difficult to separate the effect of ‘S’ phase particle removal from the matrix in decreasing the cathodic current density. According to Leclere and Newman [171] the alkalinity generated by the cathodic reduction of oxygen could activate the Al-Cu matrix and therefore the measured current is actually a net current and does not represent the true rate of the cathodic reaction.

So, to avoid any contribution from the activated aluminium-copper alloy matrix during the cathodic polarization scans and to get the true rate of cathodic reaction, further experiments of the AA2024-T351 samples with and without ‘S’ phase particles were performed in buffer solution. Two different buffer solutions were selected as discussed in Chapter 3 (Experimental Procedure) [171, 303]. In both cases the pH of the solution was 7 where the passive film of the alloy is stable. Figure 4.11(a) shows the cathodic scans in 0.1 M H_3BO_3 solution adjusted to pH 7 by the addition of 1M NaOH. It can easily be seen from the figure that removal of ‘S’ phase particles by $CeCl_3$ treatment decreases the cathodic reactivity of the alloy. Figure 4.11(b) shows the cathodic scans in another buffer solution of 0.1 M Na_2HPO_4 adjusted to pH 7 by the addition of 4M H_3PO_4. Decrease in the cathodic reactivity after the removal of ‘S’ phase particles can also clearly be found from these scans.

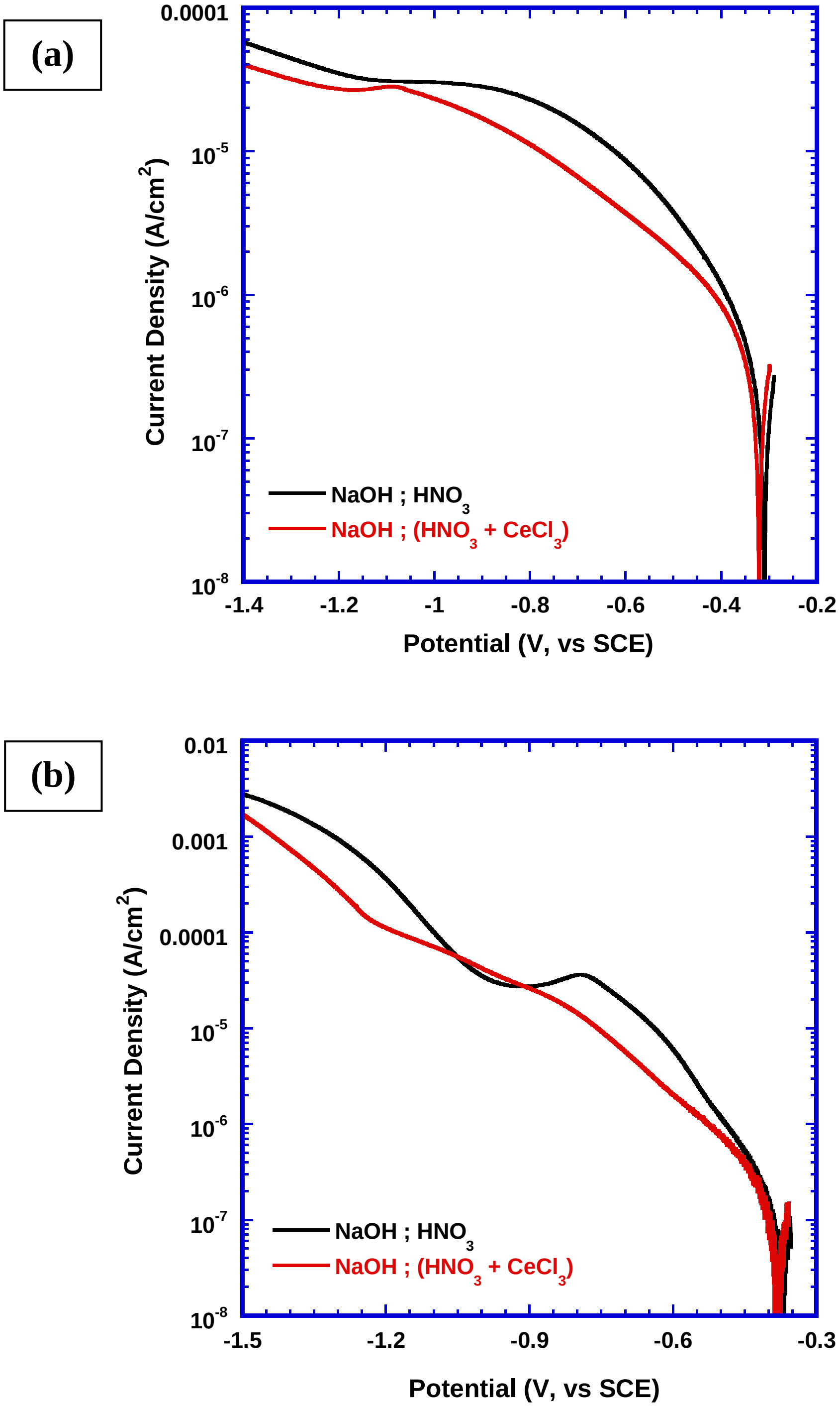

Figure 4.11 Cathodic polarization scans of AA2024-T351 in buffered solution (scan rate = 1 mV/s), (a) in 0.1 M H_3BO_3 adjusted to pH 7 by 1M NaOH and (b) in 0.1M Na_2HPO_4 adjusted to pH 7 by 4M H_3PO_4. In both cases, 'S' phase particle removed samples (with $CeCl_3$ addition) show lower cathodic reactivity than the samples having 'S' phase particles.

4.5 Open Circuit Potential (OCP) Measurements

4.5.1 Short Term OCP measurements

Short term OCP measurement of the AA2024-T351 samples desmutted with HNO_3 and with HNO_3 + 10mM $CeCl_3$ were performed in naturally aerated 10 mM NaCl Figure 4.12. The main objective of this short term exposure is to capture the initial potential fluctuations with high data collection frequency and to analyze the sample surface with optical microscopy after the experiment. Samples exposed for short times have less chance of generating a layer of corrosion products on the surface and so it is possible to take micrographs of the attack morphologies.

Figure 4.12 shows the variations in the open circuit potentials as a function of time for samples with ‘S’ phase particles (desmutted with HNO_3) and without ‘S’ phase particles (desmutted with HNO_3 + 10 mM $CeCl_3$). It can be seen from the figure that samples desmutted with HNO_3 have a lot of transients/fluctuations in the OCP, whereas samples desmutted with HNO_3 + 10 mM $CeCl_3$ show very smooth OCP curve. The transients/fluctuations in the OCP are thought to be correlated with the corrosion process on the sample surface. Samples desmutted with HNO_3 has shown few sudden drops in potentials (e.g., at ~ 700 and ~ 950 s) which are indicative of pitting corrosion. HNO_3 + 10 mM $CeCl_3$ desmutted samples show lower open circuit potential initially, but after about 400 s the OCP value starts to increase and becomes similar to that of the HNO_3 desmutted samples (~ - 500 mV vs. SCE).

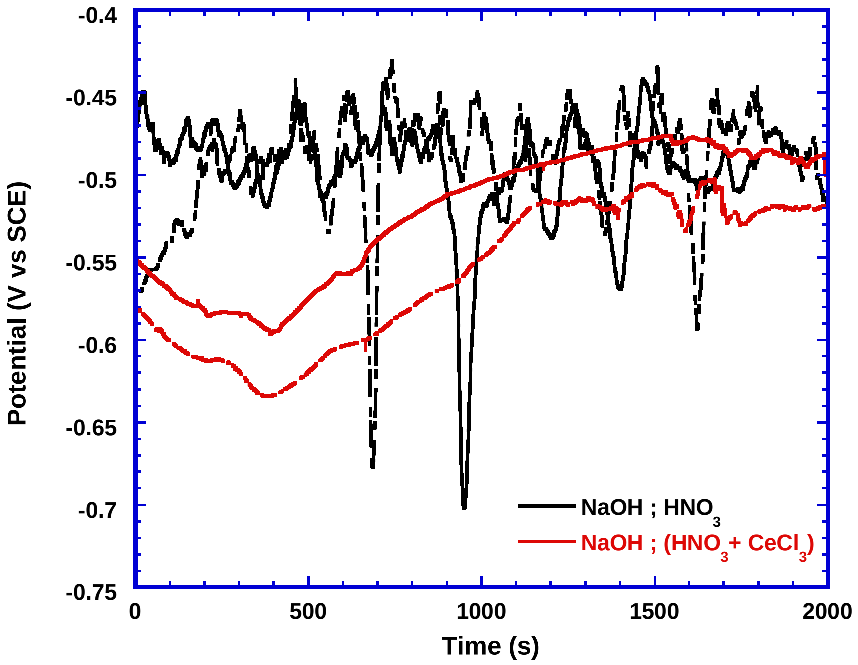

Figure 4.12 Open Circuit Potential (OCP) measurements of AA2024-T351 samples with different surface treatment in naturally aerated 10 mM NaCl. 'S' phase particle removed samples (with $CeCl_3$ addition) show less fluctuation in the potential than the samples having 'S' phase particles.

Optical micrographs of the exposed samples with both treatments are shown in Figure 4.13. It is quite clear from the micrographs that the surface of the $CeCl_3$ treated sample (without 'S' phase particle, Figure 4.13b) is relatively more shiny than the surface of the sample with 'S' phase particle (desmutted with only HNO_3, Figure 4.13a). Dealloyed particles on the sample surface could appear as black spots. It should be noted that some of the black spots on the sample surface might have resulted from the pitting attack on the sample. Rings (possibly due to the presence of acidic area around a pit) around some of the black spots are an indication of pitting attack on the surface. However, it was difficult to distinguish the black spots as pitting or dealloyed particle through the optical microscope. The sample desmutted with only HNO_3 still have 'S' phase particles present in the matrix and these ‘S’ phase particles might get attacked during the open circuit holding resulting in the small black marks in the sample surface.

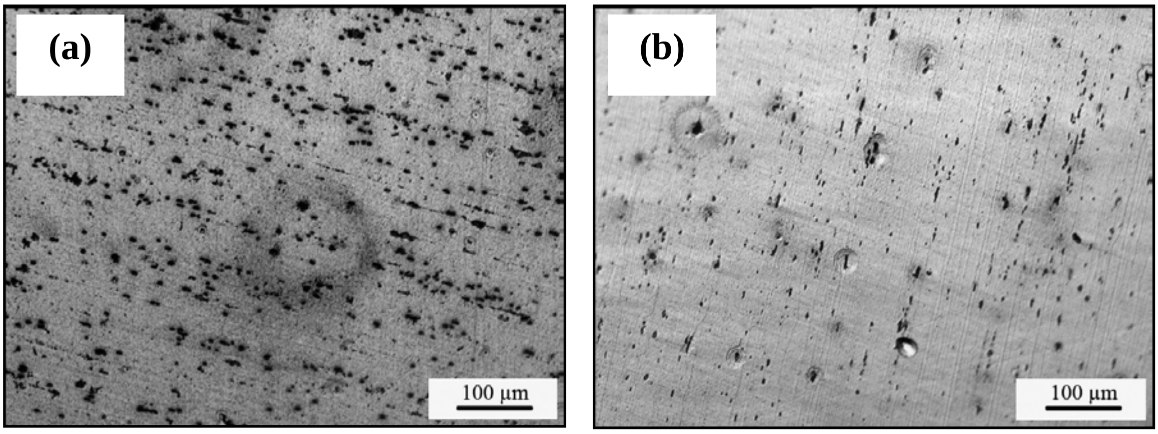

Figure 4.13 Optical micrographs of AA2024-T351 after OCP measurements for one hour in 10 mM NaCl (a) Desmutted with HNO_3, (b) Desmutted with HNO_3 + 10 mM $CeCl_3$. ‘S’ phase particle removed samples (with $CeCl_3$ addition) show fewer black spots (which could be dealloyed particles) on the surface than the samples having ‘S’ phase particles.

4.5.2 Long Term OCP Measurements

AA2024-T351 samples desmutted with HNO_3 and with HNO_3 + 10 mM $CeCl_3$ were exposed to naturally aerated 10 mM NaCl for four days. Variations of the open circuit potential of the exposed samples for the first three days are represented in Figure 4.14. The exposed sample area was about 1.2 cm^2 and experiments were performed in duplicate. It can be seen from Figure 4.14 that the open circuit potentials of the samples with different treatments are almost the same in the beginning of the test. However, close examination of the data during the first 6000 s reveals that samples desmutted with HNO_3

show many more transients/fluctuations as compared to the samples desmutted with HNO_3 + 10 mM $CeCl_3$ (similar to the Figure 4.12).

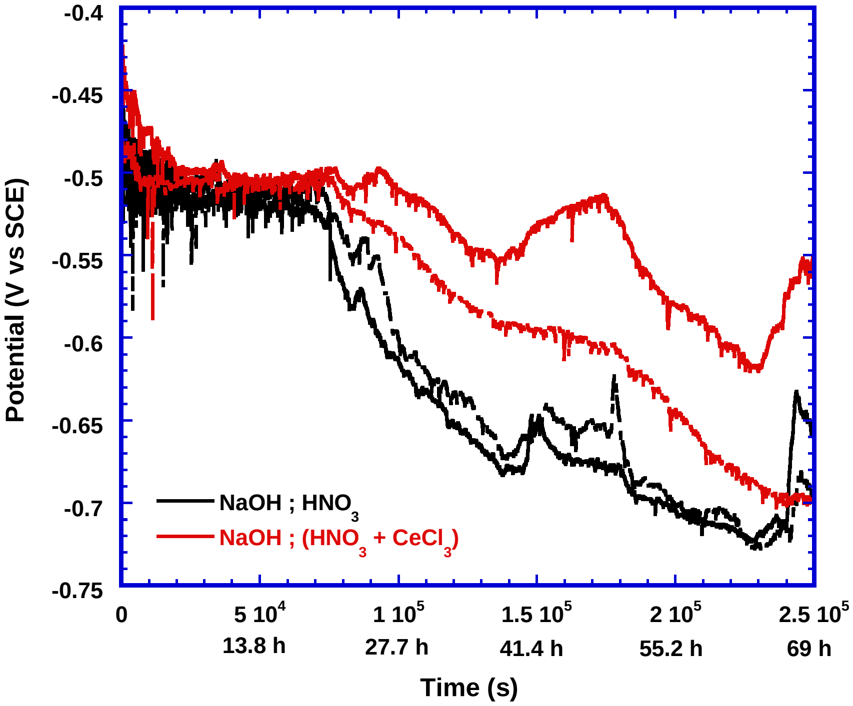

Figure 4.14 Long term Open Circuit Potential measurements of AA2024-T351 samples with different treatment in naturally aerated 10 mM NaCl. Initial potential fluctuations in the samples having 'S' phase particle (without $CeCl_3$ addition) are higher and they also show rapid decrease in the potential after ~20 h of immersion.

After about 20 hours of exposure, sharp decreases in the potential of the HNO_3 desmutted samples can be seen from Figure 4.14. This rapid decrease in the potential is associated with the occurrence of corrosion on the sample surface. The rate of decrease of the open circuit potential of the HNO_3 + 10 mM $CeCl_3$ desmutted samples is slower than the HNO_3 desmutted samples and this is an indication of the beneficial effect of 'S' phase particle removal. Within the first three days of exposure the OCP of HNO_3 desmutted samples decreased from ~ -500 mV to ~ -700 mV vs. SCE. After approximately ~66 hrs of exposure a sudden increase in the potential of one the HNO_3 desmutted samples and gradual increase in one HNO_3 + 10 mM $CeCl_3$ desmutted samples can be observed. This could probably be due to the formation of a scale of corrosion product on the corroding surface.

After the test, the samples were found to be covered with white corrosion product. Macrographs of the corroded samples are shown in Figure 4.15. Visual observations showed some difference in sample appearance between the samples desmutted with HNO_3 and the samples desmutted with HNO_3 + 10 mM $CeCl_3$. Continuous corrosion product cover can be seen on top of the HNO_3 desmutted samples [Figure 4.15(a)] whereas corrosion product seems to be discontinuous in some parts of the samples desmutted with HNO_3 + 10 mM $CeCl_3$. It was attempted to remove the corrosion product from the samples by cleaning with 70% (15.8 N) HNO_3 [304]. However, the corrosion product remained unattacked even after cleaning in HNO_3 as it can be seen from Figure 4.15. Typical optical micrographs of the exposed samples after cleaning are shown in Figure 4.16. Pitting could be observed on both types of samples as black spots on the surface beneath the corrosion product layer. Ideally the cathodic regions should be enriched with copper as a result of dealloying and should be seen as copper coloured areas under the microscope. In contrast, the anodic regions are acidic in nature and are expected to appear shiny in the microstructure.

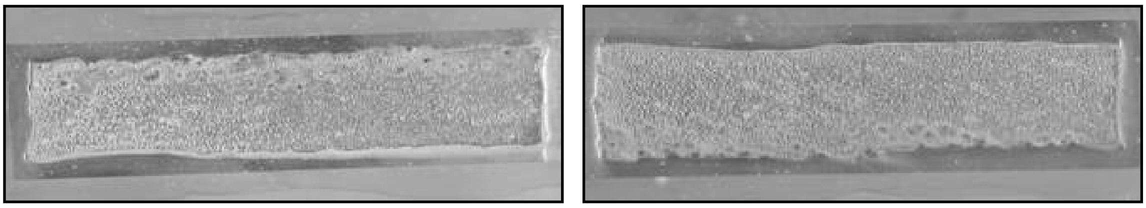

(a) NaOH ; HNO_3

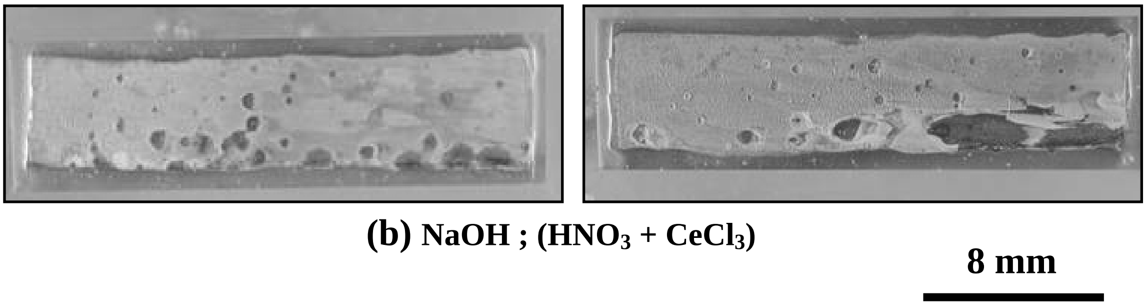

(b) NaOH ; (HNO_3 + $CeCl_3$)

Figure 4.15 Macrographs of AA2024-T351 samples after OCP measurements for 97 hour in naturally aerated 10 mM NaCl. Exposed samples were cleaned in HNO_3 before taking the macrographs. (a) Samples were desmutted with HNO_3 (with 'S' phase particles), (b) Samples were desmutted with HNO_3 + 10 mM $CeCl_3$ (without 'S' phase particles). Unattacked corrosion product can be seen on the sample surface even after cleaning in both cases.

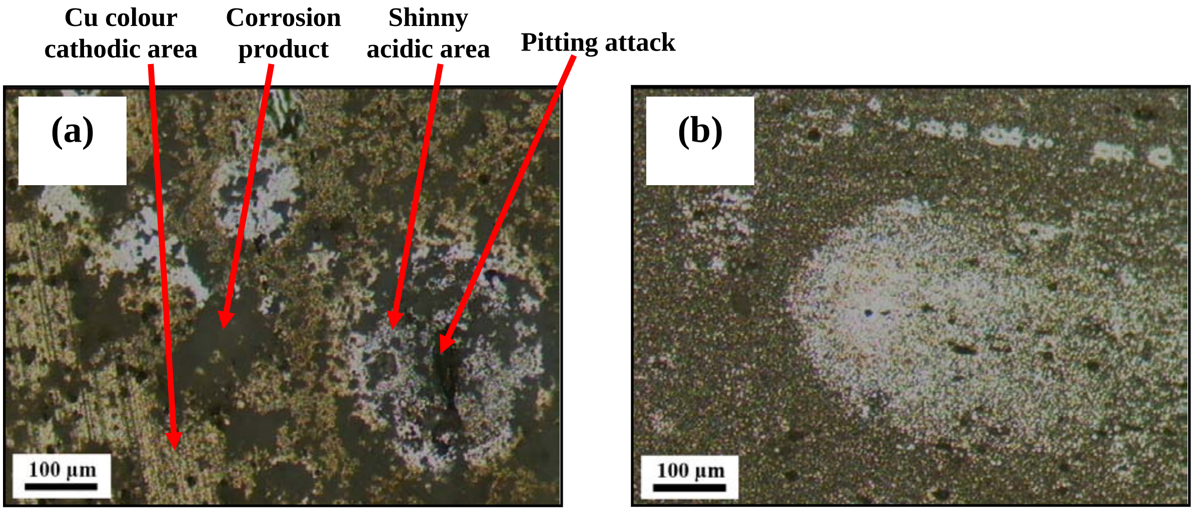

Figure 4.16 Optical micrographs of AA2024-T351 after OCP measurements for 97 hours in naturally aerated 10 mM NaCl. Exposed samples were cleaned in HNO_3 before taking the micrographs. (a) Desmutted with HNO_3 (with 'S' phase particles), (b) Desmutted with HNO_3 + 10 mM $CeCl_3$ (without 'S' phase particles).

4.6 Potentiostatic Polarization Measurements

Aluminium alloys exhibit metastable pitting and then passivation or finally stable pit growth when they are exposed in chloride environment [112, 158, 159]. Metastable pits initiate and grow for a limited period before repassivating and are believed to play crucial role in the subsequent corrosion process. The role of metastable pitting before stable pit growth thus became a topic of interest to researchers in recent years [134, 158].

In this current study, efforts have been made to find the effect of ‘S’ phase particle removal (with HNO_3 + 10 mM $CeCl_3$ desmutting) on the metastable and subsequent stable pitting. Several experiments were performed in both aerated and deaerated conditions to distinguish metastable activities and the results are presented in the following sections.

4.6.1 Potentiostatic Experiments in Deaerated 10 mM NaCl

Based on the potentiodynamic scans in deaerated conditions (Figure 4.9), different potentials were chosen for the potentiostatic experiments. As in the deaerated condition the samples showed a definite passive range, potentiostatic experiments were performed at potentials in the passive range and close to breakdown. Experiments were mainly conducted on samples desmutted with HNO_3 (with and without the addition of 10 mM $CeCl_3$ in the desmut bath) at potentials of -600 mV, -575 mV, -550mV, -525 mV and -500 mV vs. SCE. A very small surface area of 0.01 cm^2, one micron surface finish and a sampling frequency of 10 Hz was used for these experiments.

Figure 4.17 shows the comparison of the potentiostatic polarization tests of the samples desmutted with HNO_3 and with HNO_3 + 10 mM $CeCl_3$ when held at -575 mV vs. SCE in the deaerated condition. This holding potential is very close to the breakdown potential found during the potentiodynamic scans in deaerated condition (Figure 4.9) of the sample desmutted with HNO_3. It can clearly be seen from the Figure 4.17 that removal of 'S' phases (with HNO_3 + 10 mM $CeCl_3$ desmutting) helps in minimizing the metastable activities. At -575 mV vs. SCE, the sample desmutted with HNO_3 showed current transients associated with metastable pitting, whereas the current vs. time plot for the samples desmutted with the addition of 10 mM $CeCl_3$ stays flat, indicating the absence of metastable activity.

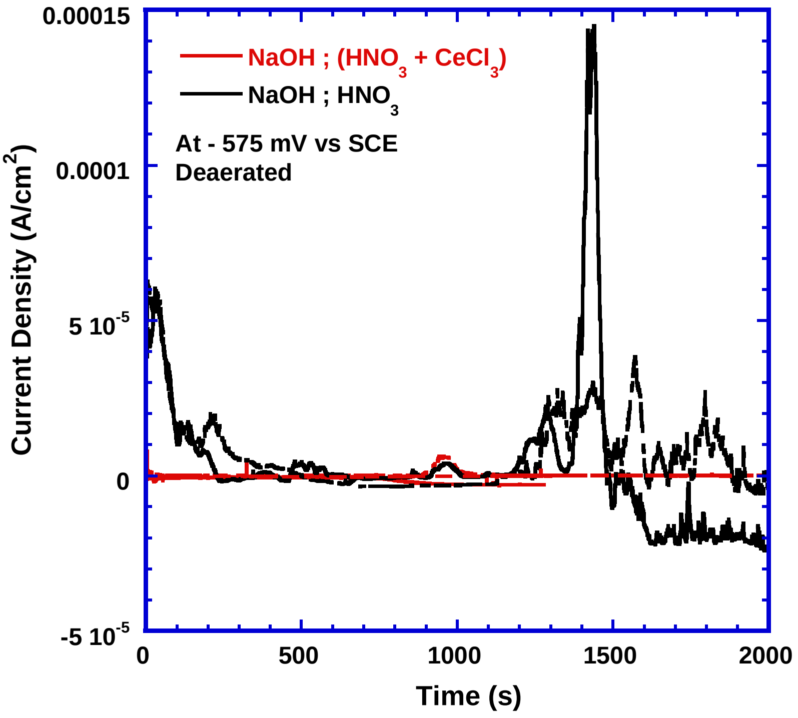

Figure 4.17 Potentiostatic polarisation at -575 mV vs. SCE in deaerated 10 mM NaCl showing the effect of 'S' phase removal from AA2024-T351. Sample having 'S' phase particles (without $CeCl_3$ addition) are showing more fluctuations in the current due to corrosion activities than the samples having no 'S' phase particles on the surface (i.e., with $CeCl_3$ addition).

Optical micrographs of the samples after the potentiostatic tests at -575 mV SCE are shown in Figure 4.18. Figure 4.18(a) [with ‘S’ phase particles] clearly show more black spots on the surface (possibly resulting from the dealloyed particles or pitting attack) than Figure 4.18(b) [without ‘S’ phase particles]. So, these observations are consistent with the electrochemical data presented in Figure 4.17.

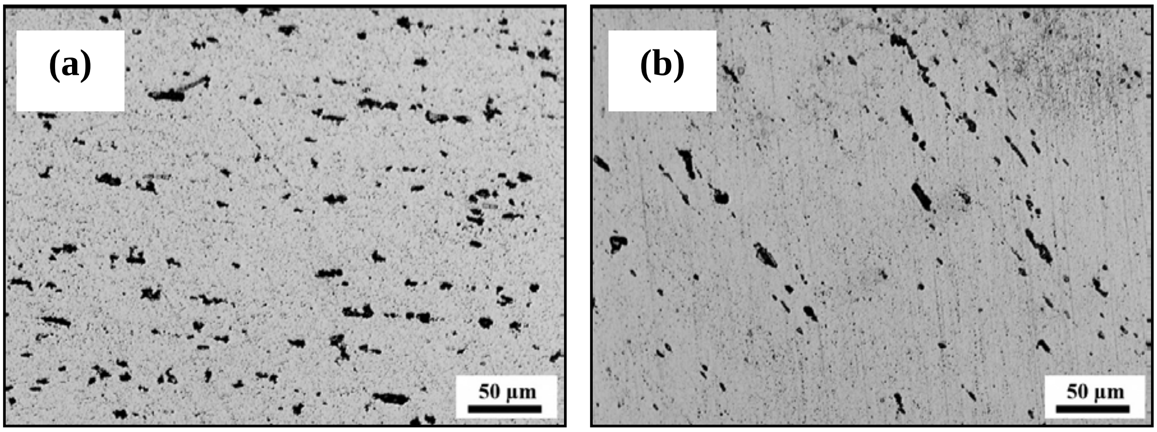

Figure 4.18 Optical micrographs of AA2024-T351 after potentiostatic polarisation scans at -575 mV vs. SCE in deaerated 10 mM NaCl (a) Desmutted with HNO_3 (with ‘S’ phase particles), (b) Desmutted with HNO_3 + 10 mM $CeCl_3$ (without ‘S’ phase particles).

Comparison of the current evolution as a function of time between the samples with and without ‘S’ phases have been made at two other different holding potentials (Figure 4.19). It can easily be seen that at both potentials (-550 mV and -500 mV vs. SCE), samples desmutted in HNO_3 + 10 mM $CeCl_3$ (without ‘S’ phase particles) shows stable current behaviour compared to the samples desmutted in HNO_3 (with ‘S’ phase particles). At a potential of -550 mV vs. SCE [Figure 4.19(a)] samples with ‘S’ phase particles show many current transients associated with metastable activities.

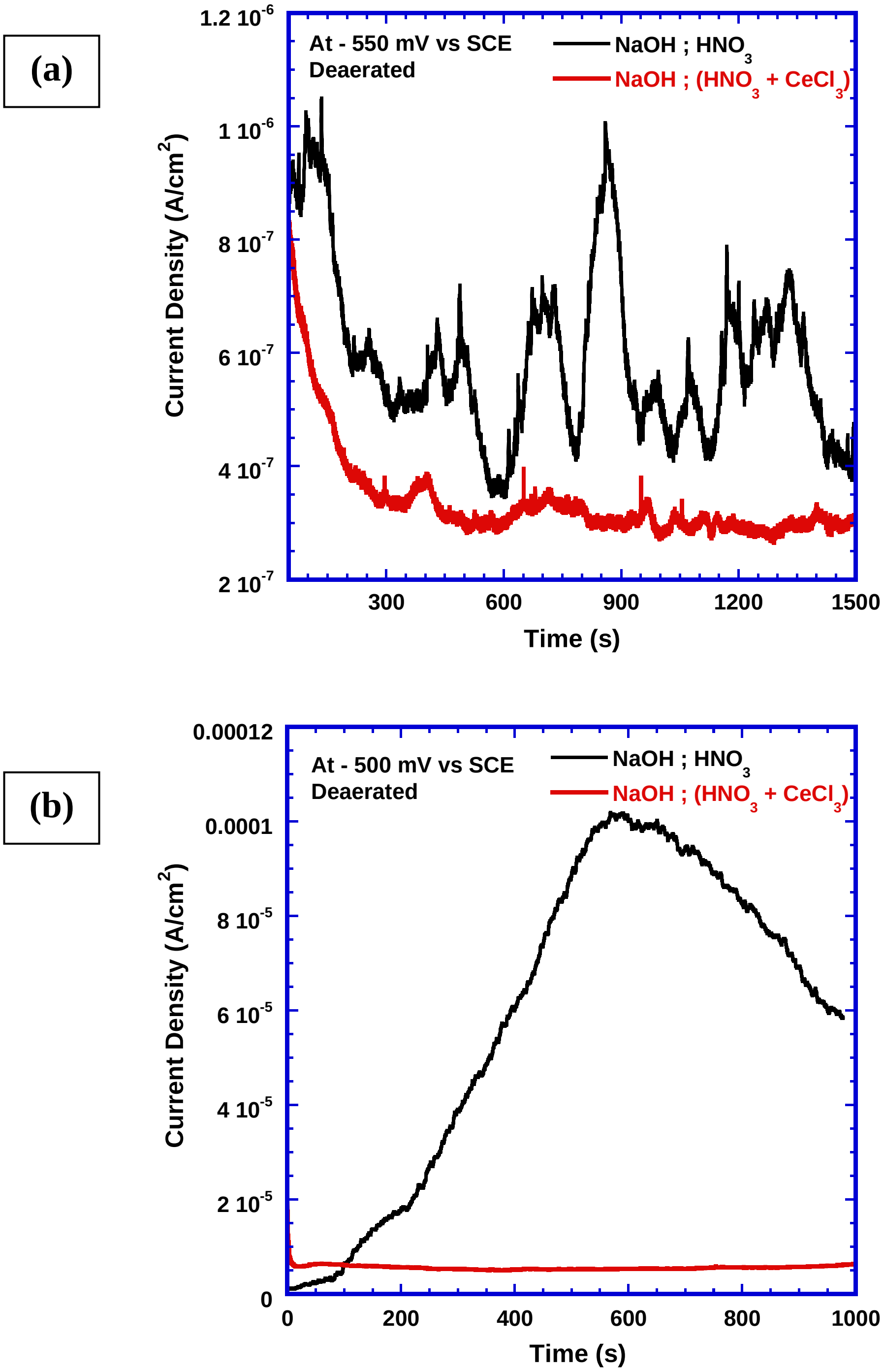

Figure 4.19 Potentiostatic polarisation of AA2024-T351 in deaerated 10 mM NaCl (a) At -550 mV vs. SCE and (b) At -500 mV vs. SCE showing the effect of 'S' phase particle removal. At both potentials, samples without 'S' phase particles (i.e., with addition of $CeCl_3$) show better corrosion performance than the samples with 'S' phase particles (i.e., without addition of $CeCl_3$ in the desmut bath).

Rapid increase in the current associated with the stable pitting can be seen in the samples with ‘S’ phase particles at a potential of -500 mV vs. SCE [Figure 4.19(b)]. Samples without ‘S’ phase particles do not show any rapid increase in the current as it is seen for the sample with ‘S’ phase particles.

So, it is quite clear from the potentiostatic scans at different potentials [Figure 4.17 and Figure 4.19] that removal of ‘S’ phase particles minimizes the metastable activities and the current transients are normally more frequent in the samples desmutted in HNO_3 (with ‘S’ phase particles). Figure 4.20 shows such metastable activities in HNO_3 desmutted sample at a holding potential of -575 mV vs. SCE. A series of transients associated with metastable pitting can be found here. A net negative current in Figure 4.20 could be due to the reduction of residual oxygen present in the solution.

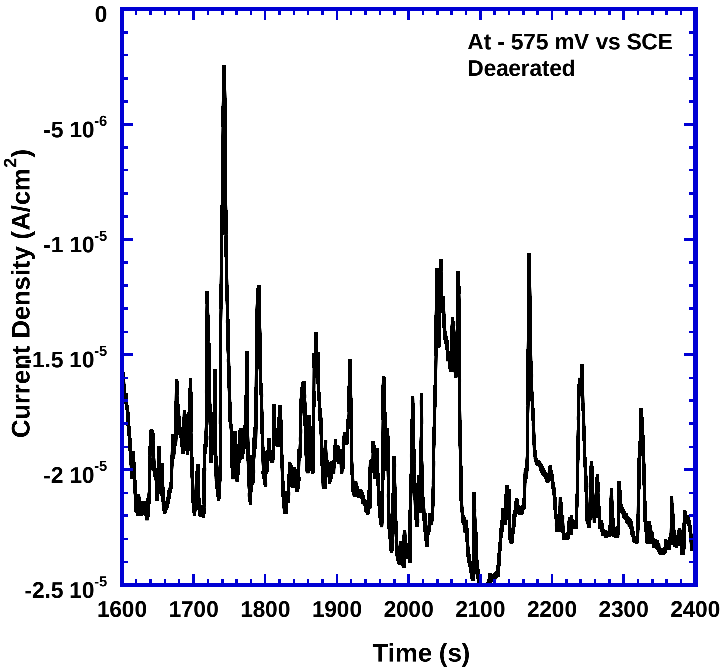

Figure 4.20 Metastable pitting of AA2024-T351 sample [first etched in NaOH and then desmutted with HNO_3 (i.e., with ‘S’ phase particles on the surface)] held at -575 mV vs. SCE in deaerated 10 mM NaCl.

Metastable pits are calculated to be in the size range of 2-8 µm in diameter (assuming hemispherical pits; calculation of pit size from the charge passed during a specific current transient is described earlier in Chapter 3). For example, the transient between 1735 s and 1754 s represents a hemispherical pit of 6.4 µm in diameter; another transient between 1977 s and 1985 s represents a hemispherical pit of 2.8 µm in diameter. However, a few larger pits are also found from this particular scan. Due to the presence of pre-existing holes in the matrix, different intermetallic particles and holes due to the dissolved ‘S’ phase particles, it was difficult to correlate the calculated metastable sizes with the microstructural observations.

4.6.2 Potentiostatic Experiments in Naturally Aerated 10 mM NaCl

It has already been seen that potentiodynamic polarization scans of AA2024-T351 with different treatments did not show any definite passive region in aerated 10 mM NaCl (Figure 4.8). So, it was difficult to choose a series of potential for potentiostatic tests and show the difference between the samples desmutted with HNO_3 (with ‘S’ phase particles) and desmutted with HNO_3 + 10 mM $CeCl_3$ (without ‘S’ phase particles). Potentiostatic experiments in deaerated 10 mM NaCl solution (Figure 4.17 and Figure 4.19) showed that samples desmutted with HNO_3 (with ‘S’ phase particles) had more tendency to exhibit metastable transients and activities than the samples without ‘S’ phase particles. So, further potentiostatic experiments in aerated 10 mM NaCl were performed on samples with ‘S’ phase particles to find out the transition from metastable to stable pitting and if oxygen played any role in changing the metastable behaviour of the alloy.

Figure 4.21 shows the metastable activities of the AA2024-T351 sample desmutted with HNO_3 at potential of -500 mV vs. SCE in aerated 10 mM NaCl. The metastable activities in the aerated condition are easily distinguishable and the current transients are not clustered together. A net negative current is likely to be due to the oxygen reduction reaction. AA2024-T351 samples with 'S' phase particles (i.e., desmutted with HNO_3) show less metastable pitting transients in the aerated condition (Figure 4.21) compared with the deaerated condition (Figure 4.20).

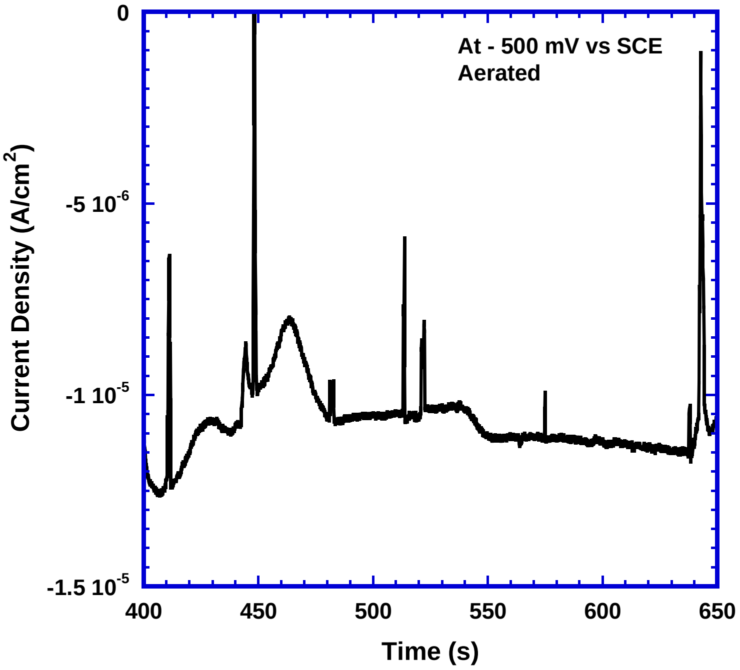

Figure 4.21 Metastable pitting of sample desmutted with HNO_3 (i.e., with 'S' phase particles on the surface) held at -500 mV vs. SCE in naturally aerated 10 mM NaCl. Each current transients are associated with metastable pitting activities.

It should be emphasized that, this comparison deals with two potentiostatic polarizations experiments at two different potentials. However, this comparison could still be valid as the frequency of metastable pitting transients in both cases are compared and clear metastable activities have been seen at two different potentials in aerated vs.

deaerated solution (i.e., -575 mV vs. SCE for deaerated condition and -500 mV vs. SCE for aerated condition). Metastable activities in the aerated condition are less even at a higher potential (i.e., at -500 vs. SCE) as compared with the deaerated condition (i.e., at -575 vs. SCE).

Figure 4.22 shows the shape of a typical metastable pit current peak. A rapid increase in the current (at time t_i) occurs on the onset of metastable pitting and at t_{max} the peak current I_{peak} is reached. The metastable pit can not sustain its growth, so repassivation starts at t_{max} and finish at t_f where the current return to its base value (i.e., passive current I_{ox}). Based on the charge passed from time t_i to t_f (in Figure 4.22), the diameter of the metastable pit is calculated to be about 2.3 µm.

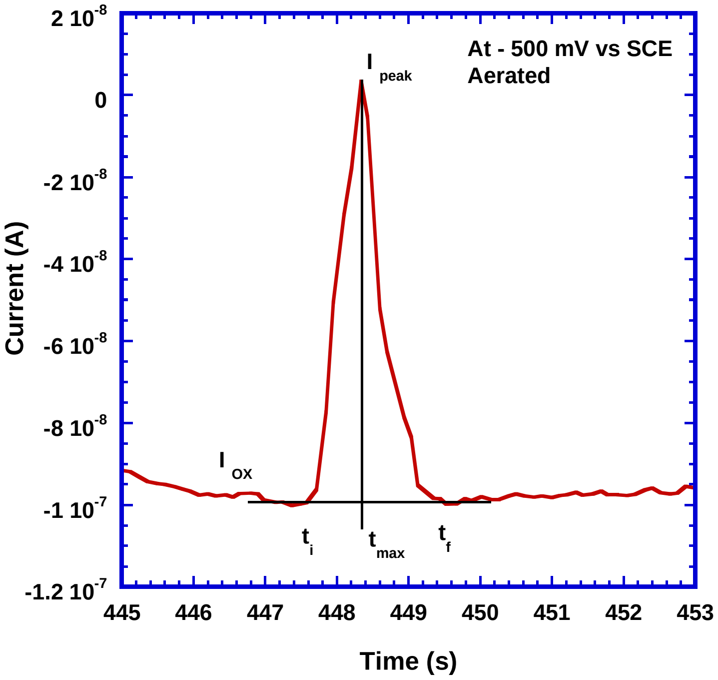

Figure 4.22 Analysis of a single metastable pit of the AA2024-T351 sample desmutted with HNO_3 (i.e., with 'S' phase particles on the surface) held at -500 mV vs. SCE in naturally aerated 10 mM NaCl. Total charge under such current transients can be calculated to find out the metastable pit size assuming hemispherical pit geometry.

Several other metastable pit sizes are also calculated from Figure 4.21. Metastable pit diameter between 410.2 s (t_i) and 411.9 s (t_f) is calculated to be approximately 2 µm. Analysis showed that in deaerated solution metastable pits were approximately 2-8 µm in diameter, whereas aerated experiments results in metastable pits of 1-4 µm in diameter. These results on the alloy 2024-T351 are consistent with the findings of Pride *et al.* [134, 167] who reported metastable pitting in the same size range.

4.6.3 Role of Oxygen in Metastable Pitting

Comparison of the potentiostatic polarization scans in the deaerated and aerated conditions as described in the earlier sections suggest that oxygen might play an important role in the metastable pitting activities. The presence of oxygen in the system seems to reduce the frequency of metastable pitting transients (comparison between Figure 4.20 and Figure 4.21). The role of oxygen in reducing metastable activities is clearly established in Figure 4.23 which shows the comparison of the potentiostatic tests of AA2024-T351 samples desmutted in HNO_3 in deaerated and aerated 10 mM NaCl at a holding potential of -575 mV vs. SCE.

The initial increase in the current in both deaerated and aerated condition is associated with the initiation of the localized attack. However, the subsequent decrease in the current indicates that the localized attack does not propagate further. It is quite clear from Figure 4.23 that metastable activities in the deaerated condition are more prominent than in the aerated condition. After the initial decay, the current stays flat in the aerated condition, whereas significant amount of current transients associated with metastable pitting can be seen in the deaerated condition.

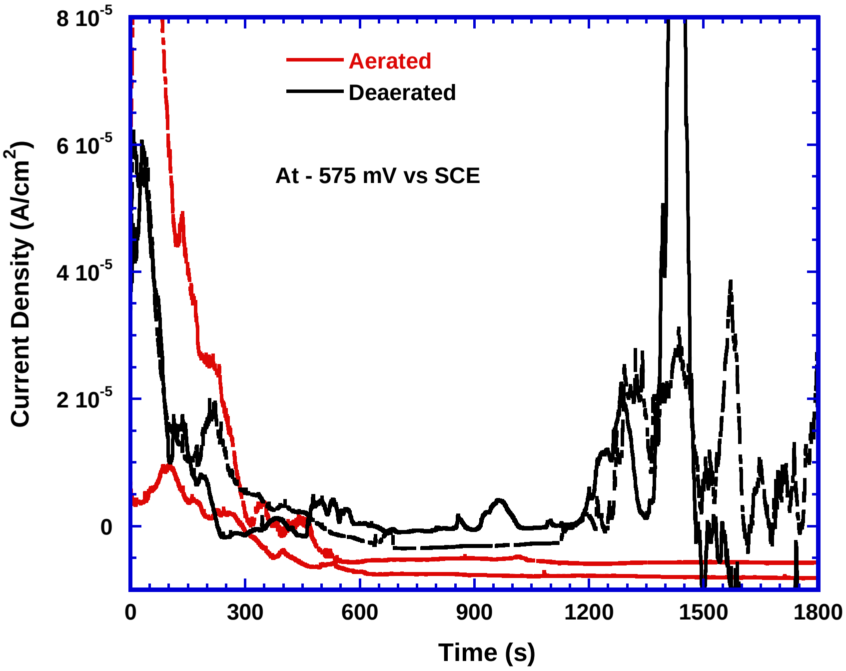

Figure 4.23 Comparison of the potentiostatic polarization of AA2024-T351 samples desmutted with HNO_3 (i.e., with 'S' phase particles on the surface) in deaerated vs. naturally aerated 10 mM NaCl solution at -575 mV/SCE. Deaerated samples show more current transients indicating more corrosion activities on the surface than the samples in the aerated condition.

The presence of oxygen may enhance the oxygen reduction reaction and thereby increase the local alkalinity. This increase in the local alkalinity therefore may suppress the local acidity associated with metastable pitting and help them to repassivate quickly. So, few controlled experiments were performed with AA2024-T351 samples desmutted with HNO_3 + 10 mM $CeCl_3$ (without 'S' phase particles) with the addition of deaerated and aerated solution during the potentiostatic polarization at -520 mV vs. SCE. Samples were polished to one micron and the potentiostatic holds were started in deaerated 10 mM NaCl. Current evolution as a function of time during these tests with the addition of deaerated and aerated solution at different stages of tests is shown in Figure 4.24. Current spikes or transients associated with the metastable pitting can be seen at the very beginning of the potentiostatic tests in deaerated solution at -520 mV vs. SCE. After 100 seconds deaerated solution was added in the system (details of the procedure can be found in Chapter 3). Addition of deaerated solution in the system did not change the metastable behaviour of the sample and a gradual increase in the current continued. After the addition of first portion of aerated solution in the system, metastable pitting started becoming less frequent and after the final portion of aerated solution was added, the current started decreasing and only a very few current transients were observed thereafter.

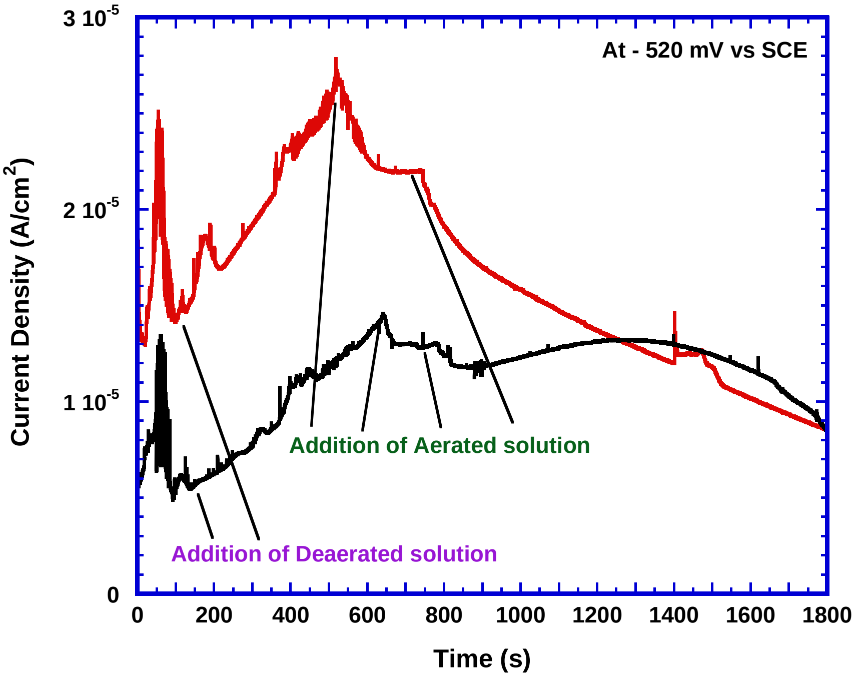

Figure 4.24 Potentiostatic polarization of AA2024-T351 samples desmutted with HNO_3 + 10 mM $CeCl_3$ (i.e., without 'S' phase particles on the surface) at -520 mV vs. SCE. Samples were tested in deaerated 10 mM NaCl while deaerated and aerated 10 mM NaCl was added during the test.

4.7 Discussion

In this current study, two predominant categories of constituent intermetallics particles have been identified in AA2024-T351 (Section 4.1). The first type is irregular in shape and in the size range of 10-30 µm containing mainly Al-Cu-Fe-Mn (mentioned as "Fe-Mn" particle throughout the study). Several other researchers [9, 11, 45, 56, 57, 72-77, 204] have also documented presence of such type of coarse intermetallic particles in AA2024 and therefore findings from the current study is consistent with those reported earlier. In many cases, Fe-containing intermetallic particles are broken down in fragments during subsequent thermo-mechanical treatment as seen in Figure 4.1(b) [7, 8, 81]. The Fe-containing intermetallic particles from this present study seem to follow a stoichiometric relationship close to $Al_{15}Cu_3(Fe,Mn)$ [Table 4.1]. Very few Fe-containing intermetallic particles in this current study have been found to have Si in it.

However, it should be noted that different batches of AA2024-T3 can have different Si content and as a result some of the alloys reported in the literature show Fe-rich intermetallic particles with Si and some other do not. For example, Chen *et al.* [8] and Buchheit *et al.* [9] did not report the presence of Fe-rich intermetallic particle with Si in AA2024-T3, whereas Campestrini [6] found Si containing Fe-rich intermetallic particles in their study. Buchheit *et al.* [9] found that the ratio of Al to the sum of Cu, Fe, and Mn was regularly 6 to 1 on an atomic percentage basis during their EDS analysis. The average Cu:Fe:Mn ratio was 2:1:1 and varied little from particle to particle. Hence they assigned the second largest category of Al-Cu-Fe-Mn particles to be chemically the $Al_6(Cu,Fe,Mn)$ type. However, this current study emphasizes the fact as pointed out by other researchers [7, 75] that the Fe-containing intermetallic particles may not possess any definite stoichiometric relationship. Therefore, Fe-rich intermetallic particles in this current study are referred as Fe-Mn phase/particles. Some of the Fe-Mn particles contain more copper than the others as it is indicated by the relatively high standard deviation in the copper content (Table 4.1 and Figure 4.3).

The second type of coarse intermetallic/constituent particle appeared as round and smooth with a size range of 1-5 µm and were identified as Al_2CuMg (‘S’ phase). The number of ‘S’ phase particles in the matrix of AA2024-T351 are much higher that the Fe-Mn particles. These findings are consistent with the literature as reported by several researchers [5-9, 11, 19, 43-45, 70, 76, 80, 174, 198, 204, 211, 315]. In a few occasions ‘S’ phase particles are found to be in an elongated shape and as large as ~10 µm in size. A small number of rounded and smooth particles are seen to contain Al and Cu. EDS analysis show that stoichiometric of the Al-Cu particles are very close to Al_2Cu and therefore consistent with the findings of other researchers [75]. These Al_2Cu particles are small, rounded (1-2 µm) and generally found as isolated individual particles.

Intermetallic particles like ‘S’ phase particles and Fe-Mn particles play a crucial role in determining the corrosion behaviour of AA2024-T351. Several researchers have shown that pitting corrosion in aluminium alloys is normally associated with the intermetallic particles [8-11, 14, 37, 38, 40, 42, 47, 48, 82, 123, 171, 173, 175, 181-197]. It is believed that Fe-Mn intermetallic particles generally act as cathode during the corrosion process. Fe-Mn particles do not show selective dissolution, though pitting sometime occurs at their periphery [7, 8, 11, 175, 186, 187]. In contrast, a number of researchers have confirmed the anodic behaviour of ‘S’ phase particles by showing the initiations of pits on the particles [8, 12, 37, 43, 46, 174, 185, 198]. It has to be mentioned that, though the ‘S’ phase particles show initial anodic behaviour, they can then become cathodically active because of dealloying and subsequent copper enrichment.

Electrochemical behaviour of each type of intermetallic particles will be discussed in details in Chapter 5.

In order to find a suitable replacement for the chromate conversion coating as a pretreatment technique, much focus has been given in the surface preparation of the substrate by etching out the intermetallic particles (mostly cathodic in nature) from the surface of the aluminium alloy. The fact that the chromate conversion coating is widely used as a pretreatment technique because of its ability of inhibiting the cathodic oxygen reduction reaction on the intermetallic particles and thereby minimising corrosion [74, 249, 250], researchers have tried to maintain this advantage (i.e., improved corrosion properties and effectiveness in inhibiting the cathodic reaction) in the alternate pretreatment methods [see Section 2.3 of Chapter 2 for more details]. Hence, one of the main objectives of this chapter is to demonstrate an effective surface treatment technique for removing deleterious ‘S’ phase particles from the surface of AA2024-T351 and to investigate if the removal of ‘S’ phase particles can actually improve the corrosion resistance of the alloy.

The effect of surface treatment on the appearance of different intermetallic particles is shown in Section 4.2. It is found that addition of 10 mM $CeCl_3$ in the nitric acid desmut bath (after alkaline etching) completely removes the ‘S’ phase particles from the surface of AA2024-T351 and partially attacks the Fe-Mn particles (Figure 4.5). Desmutting only in a nitric acid bath (after alkaline etching) does not remove the ‘S’ phases from the matrix (Figure 4.4) although a few Fe-Mn particles are seen to be attacked. Etching in sodium hydroxide does not remove the intermetallic particles because in the alkaline environment Mg is stable and protects the ‘S’ phase particles. These findings are also consistent with other researchers [19, 260] who found that addition of rare earth chloride in the nitric acid bath helped in removing ‘S’ phase intermetallic particles. However, the exact mechanism behind the ‘S’ phase particle removal by the addition of $CeCl_3$ in the desmut bath is not completely understood as yet. Moulinier [19] showed that Cl^- ions are actually responsible for removing the ‘S’ phase particles, not the Ce^{3+} ions. In her study, addition of 30 mM NaCl showed similar effect to that of the 10 mM $CeCl_3$ addition in the desmut bath. But when 10 mM $Ce(NO_3)_3$ was added to the desmut bath, ‘S’ phase remained unattacked. Addition of 30 mM NaCl in the desmut bath in this current study has also shown a similar effect like 10 mM $CeCl_3$ addition. So, it has clearly been established that Cl^- ions are the actual responsible species for removing ‘S’ phase particles.

During etching in NaOH, aluminium dissolves by forming aluminate ions, $Al(OH)_4$ and copper accumulates on the surface as a black deposit. Copper can react with NaOH to form CuO which is a black oxide [see Section 2.3 for more details]. Matrix dissolution during the surface treatment procedure is found to be approximately 900nm to 1µm (Figure 4.7). This value is consistent with the findings of others [19] with similar surface treatments. Dissolution of the matrix mainly occurs during the etching process in NaOH and additions of Cl^- ions in the nitric acid desmut bath do not affect the extent of matrix dissolution [19].

A series of anodic potentiodynamic polarization scans in both naturally aerated and deaerated conditions show the beneficial effect of the surface treatment (i.e., ‘S’ phase particle removal) on the AA2024-T351 surface. In aerated condition (Figure 4.8), samples without ‘S’ phase particles show lower anodic reactivity (and subsequent higher breakdown potential) than the samples with ‘S’ phase particles. Beneficial effect of the ‘S’ phase particle removal by surface treatment can also be seen in the deaerated condition (Figure 4.9) where samples without ‘S’ phase particles (i.e., with addition of $CeCl_3$ in the desmut bath) show higher breakdown potential than the samples with ‘S’ phase particles on the surface. Interestingly, the passive current density increases after the samples are etched with sodium hydroxide. The exact reason for the higher passive current densities after the NaOH etching is not clearly understood as yet. However, the process resulting in visible dispersoids and precipitates after the surface treatment (Figure 4.4 and Figure 4.5) could play a role in increasing the passive current densities.

So, the improvement in the corrosion properties of AA2024-T351 after the ‘S’ phase particles removal in both aerated and deaerated condition establishes the deleterious effect of ‘S’ phase particles in the corrosion initiation. These findings are consistent with the researchers who identified ‘S’ phase particles as the most active phase in AA2024-T351 and referred as the key contributor for the poor corrosion resistance of AA2024-T351 [8, 9, 12, 37, 43, 46, 174, 185, 198] (further details about the corrosion performances of ‘S’ phase particles and their role in pit initiation have already been discussed in Section 2.2.1.2.1 of Chapter 2). Corrosion properties of these individual intermetallic phases using microcapillary electrochemical cell (micro-cell) technique will be discussed in details in Chapter 5. Initiation of localized corrosion in AA2024-T351 is found in the form of pitting in all cases after the potentiodynamic scans.

Localized corrosion susceptibility of AA2024-T351 could be significantly affected by the enhanced cathodic reactivity of the exposed area [70]. Addition of $CeCl_3$ in the desmut bath not only enhances the dissolution of copper rich intermetallic particles (i.e., ‘S’ phase particles) but also enhances the anodic dissolution of the copper accumulated on the surface after etching [19]. ‘S’ phase particle initially behaves anodically which results in the dealloying of Mg (and Al) from the particle. The particle will soon become rich in Cu and start acting as cathode, as Cu is a better surface for oxygen reduction. In several papers, Buchheit *et al.* [9, 14, 82, 123, 181, 182] described the phenomena of Cu distribution in the surface during the corrosion process. So, according to these observations and theories, addition of $CeCl_3$ in the desmut bath should result into the decrease in the cathodic reactivity of the AA2024-T351 as it removes the ‘S’ phase particles from the microstructure. Findings in this current study are consistent with the proposed theories of other researchers as the addition of 10 mM $CeCl_3$ in the desmut bath reduce the cathodic reactivity of the AA2024-T351 sample (Figure 4.10).

Decrease in the cathodic reactivity after the removal of ‘S’ phase particles in this current study is confirmed after the cathodic polarization scans in two different buffer solutions (Figure 4.11). As discussed earlier, the increase in local alkalinity due to the oxygen reduction reaction dissolves the passive film and exposes bare alloy surface which also might affect the cathodic current densities. The use of buffer solution suppresses the possibility of local alkalinity change and hence represent the true rate of the cathodic reaction [171].

Open circuit potential (OCP, also referred as corrosion potential) measurements of the surface treated AA2024-T351 samples without and with addition of 10 mM $CeCl_3$ in the desmut bath also proves the beneficial effects of ‘S’ phase particle removal from the surface. Samples with ‘S’ phase particles (i.e., without addition of $CeCl_3$) show more fluctuations in the corrosion potential resulting from the corrosion activities (metastable and stable pitting) on the surface (Figure 4.12 and Figure 4.13).

In chloride environments aluminium alloys exhibit metastable pitting and then passivation or finally stable pit growth [112, 158, 159]. A number of researchers have confirmed the anodic behaviour of ‘S’ phase particle by showing the initiations of pits on the particles [8, 12, 37, 43, 46, 174, 185, 198]. So, based on these observations from different researchers, AA2024-T351 samples with ‘S’ phase particles are expected to show more metastable activities than the samples without ‘S’ phase particles. Figure 4.17 and Figure 4.19(a) prove the deleterious role of ‘S’ phase particles in initiating metastable activities (and resulting stable pitting in later stages). At two different polarization potentials during the potentiostatic tests, AA2024-T351 samples with ‘S’ phase particles show more metastable transients than the samples without ‘S’ phase particles. At a slightly higher holding potential (-500 mV/SCE), samples with ‘S’ phase particles (i.e., without $CeCl_3$ addition in the desmut bath) show stable pit growth (indicated by the rapid increase in the current density) whereas samples without ‘S’ phase particles show stable current, Figure 4.19(b).

Individual current transient associated with the metastable pitting in aerated and deaerated conditions (Figure 4.20, Figure 4.21) show that in the case of deaerated solution metastable pits are approximately 2-8 µm in diameter, whereas aerated experiments result into metastable pits of ~ 1-4 µm in diameter (assuming hemispherical pit geometry). These results on the alloy 2024-T351 are consistent with the findings of Pride *et al.* [134, 167] who also reported metastable pitting in the same size range.

However, it should be noted that finding the right conditions for capturing the metastable events during the corrosion of aluminium alloys is quite a challenging work. Metastable pitting behaviour of AA2024-T351 has not been well documented in the open literature. Metastable activities depend on many factors including alloy composition, experimental conditions, surface finish etc. Capturing the current transient depend on the sampling frequency, sample area, background noise level, applied potentials etc. [134]. Due to the presence of pre-existing holes in the matrix, different intermetallic particles and holes due to the dissolved ‘S’ phase particles, it was difficult to correlate the calculated metastable sizes with the microstructural observations. Hence, no criteria for the transition from metastable pitting to stable pitting have been established in this current study (details about the metastable to stable pitting criteria as given by other researchers can be found in Section 2.2.1.3).

In an alloy like AA2024-T3, the growth of the metastable pits depends on several factors including the locality of intermetallic cathodic sites and their related ohmic drops [158]. Galvele [114] and Pride [167] used pit stability criteria of $x.i \geq 10^{-2}$ A/cm (x is the pit depth and i is the pit current density), whereas Trueman [158] used a specific amount of charge passed (20 µC, i.e., equivalent to 13.7 µm diameter of hemispherical pit) to indicate the transition from metastable to stable pitting. But as described earlier, due to the presence of several types of microstructural features (including resulting holes after ‘S’ phase particle removal) it was difficult to identify a particular metastable pitting in a heterogeneous alloy like AA2024-T351. However, all the current transients analyzed in this current study show pit size smaller than the transition criteria (from metastable to stable pitting) set by the above mentioned researchers and thereby emphasizing the metastable nature of the pitting whose sizes are calculated in this study.

As pit initiation in aluminium alloys is normally associated with the intermetallic/constituent particles [8-11, 14, 37, 38, 40, 42, 47, 48, 82, 123, 171, 173, 175, 181-197], oxygen might play an important role in the metastable pitting activities in AA2024-T351. Most of the intermetallic particles act as favourable place for oxygen reduction (‘S’ phase particles initially behave anodically and the resulting Cu enrichment on the surface makes it a favourable site for oxygen reduction). Hence, the presence of oxygen may enhance the oxygen reduction reaction and thereby increase the local alkalinity. Evidence of the increase in the local alkalinity adjacent to the intermetallic particles is found from the presence trenching/grooving around the particles.[15] Increase in the local pH dissolves the passive film of the adjacent alloy matrix and forms a trench/groove around the particle. These type of trenching formation between the matrix

---

[15] See Chapter 5 for more details.

and the intermetallic particle has been extensively discussed in the literature [8, 40, 43, 48, 171, 175, 186, 198, 209]. Increase in the local alkalinity therefore may suppress the local acidity associated with metastable pitting and help them to repassivate quickly. The theory of suppression of pit initiation by the increase in local alkalinity in the presence of oxygen has been supported by this current study and hence consistent with the findings of Hoerlé *et al.* [316] whose proposed model provides a suitable framework for analyzing the role of local acidity in the appearance of metastable transients during the corrosion of aluminium alloys. Hoerlé's model emphasizes on the local variations in the H^+ protons as the major controlling factor during the passive/active transitions of aluminium alloys. It can be seen from this current study that the presence of oxygen in the system clearly reduces the frequency metastable pitting transients (comparison between Figure 4.20 and Figure 4.21). The role of oxygen in reducing metastable activities is clearly established in Figure 4.23 which shows that the metastable activities in deaerated condition are more prominent than in the aerated condition. Role of oxygen in metastable pitting of AA2024-T351 is elaborated further in Figure 4.24. Addition of deaerated solution in the system did not change the metastable behaviour of the sample, whereas addition of aerated solution in the system reduced metastable activities in the system.

4.8 Conclusions

1. Addition of 30 mM Cl^- (10 mM $CeCl_3$ or 30 mM NaCl) in the desmut bath of a surface treatment removes the 'S' phase intermetallic particles from the matrix of AA2024-T351. SEM analysis also shows partial attack on the Fe-Mn particles by the Cl^- ions.

2. Removal of the ‘S’ phase particles has a beneficial effect on the corrosion properties of AA2024-T351. It improves the corrosion resistance of the alloy by increasing the pitting/breakdown potential.
3. Cathodic scans in different buffer solutions showed the decrease in cathodic reactivity after the ‘S’ phase particles are removed by the addition of $CeCl_3$ in the desmut bath. This proves that the presence of ‘S’ phase particles on the alloy surface can increase the cathodic reactivity of the aluminium alloy 2024. Higher cathodic reactivity on the ‘S’ phase particles can increase the possibility of alkaline corrosion in the matrix adjacent to the particle.
4. Microscopic analysis of the samples after short term exposure in 10 mM NaCl revealed that the sample desmutted with $CeCl_3$ have shown less amount of pitting attack on the surface.
5. Metastable pitting could be observed for both samples (desmutted with and without $CeCl_3$) in appropriate experimental conditions. Removal of ‘S’ phase particles from the matrix reduces the metastable activities.
6. HNO_3 desmutted samples showed less metastable pitting transients in aerated condition compared to deaerated experiment at different potentials. Metastable activities in the aerated condition were easily distinguishable. Therefore, local increases in the alkalinity due to the oxygen reduction in aerated condition seem to inhibit pitting corrosion initiation.